Supporting information:

Characterization of Ionic-electronic Transport and Recombination in Perovskite Solar Cells under Multi-biasing Conditions

Juan Pablo Medina Flechas[1,2]*, Dounya Barrit[1,2], Raj Dashrath Patel[2], Tianfang Li[1,2], Estelle Cariou[2], Marion Provost[2], Leonardo Koppio[2,3], Sylvain Le Gall[2,3], Jean-Paul Kleider[2,3], Osbel Almora[4], Camille Bainier[1,2], Pilar Lopez-Varo[2]*, Philip Schulz[2,5]*

[1] TotalEnergies OneTech, 91120 Palaiseau, France
[2] Institut Photovoltaïque d'Ile-de-France (IPVF), 18 Boulevard Thomas Gobert, 91120 Palaiseau, France
[3] Université Paris-Saclay, CentraleSupélec, CNRS, Laboratoire de Génie Electrique et Electronique de Paris, 91192 Gif-sur-Yvette, France
[4] Department of Electronic, Electrical and Automatic Engineering, Universitat Rovira i Virgili, 43007 Tarragona, Spain
[5] Institut Photovoltaïque d'Île-de-France (IPVF), UMR 9006, CNRS, Ecole Polytechnique - IP Paris, Chimie Paristech - PSL, 18 Boulevard Thomas Gobert, Palaiseau 91120, France

* medina.juanpablo@outlook.es
* pilar.lopez-varo@ipvf.fr
* philip.schulz@cnrs.fr

S1. Experimental information

Device fabrication

Inverted (p-i-n) perovskite solar cells were deposited on glass-FTO substrates, with a NiO_x/SAMs/ $Cs_{0.05}(FA_{0.86}MA_{0.14})_{0.95}Pb(I_{0.84}Br_{0.16})_3/C_{60}/SnO_2$/Au structure. First, glass-FTO substrates were treated under a series of ultrasonic baths with detergent, deionized water, acetone, and isopropanol; followed by ultraviolet-ozone treatment for 15 min. Subsequently, a compact layer of NiO_x was deposited over the substrates (~15 nm) through atomic layer deposition (ALD) cycles at 160 °C. Organic MeO-2PACz molecules (so called "SAMs", self-assembled monolayers) were first dissolved in ethanol, then the solution of 2 mM (0.67 mg/ml) was spin-coated onto the substrates and heated at 100°C for 10 min. For the synthesis of perovskite films with 1.63 eV bandgap (E_g), precursor solutions were prepared in N2-filled glovebox by dissolving 1.5 M CsI in 250 µL of dimethylsulfoxide (DMSO) and the organic halides along with PbI_2 and $PbBr_2$ (0.2 M MABr, 1 M FAI, 0.1 M $PbBr_2$ and 1.1 M PbI_2) in 1 mL mixture of dimethylformamide (DMF) and DMSO (4:1 volume ratio). The precursors were left under agitation overnight. Then, the mixture of 42 µL of 1.5 M CsI precursor with 1mL of solution containing the mixed halides and heating at 70 °C for 1 hour before deposition. During the spin-coating, starting at a rotation of 2000 rpm, once passed 2 minutes under spin acceleration, 35 µL of the perovskite solution were dripped over the substrate and left for another 10 s. In the second step of 32 s at 6000 rpm, a volume of 100 µL of chlorobenzene was spin-cast onto the film after 12 s of rotation. Then, the perovskite film (~450 nm) was thermally annealed at 100 °C within the glovebox for 30 min. The C_{60} overlayer (~15 nm) was deposited by thermal evaporation and the SnO_2 (~15 nm) via ALD. 100 nm of gold (Au) were deposited as top contact electrode, using a mask for a final device' active area of 0.20 mm².

Opto-electric characterization

Current-voltage (*J–V*) curves at 1 sun AM1.5G equivalent illumination were measured without mask shading, using a Newport Oriel solar simulator (Xenon lamp) calibrated using a silicon+KG5 reference cell, in reverse (RV) and forward (FW) scan direction at a rate of 30 mV/s. Dark *J–V,* SunsVoc and IS measurements were performed in open air using an integrated Zahner CIMPS-EQE/IPCE electrochemical station composed of two main Zennium Pro and PP212 potentiostats, with a Faraday box for electromagnetic isolation (see **Fig. S1**) containing: (i) a white LED (4300 K) with rated power of 140 $mWcm^{-2}$ (1.4 sun); and (ii) another tunable monochromatic light source (TLS03/UV) in the 295 – 1020 nm range.

SunsVoc and IS were performed at different voltage bias (J_{SC} then V_{OC}) under increasing illumination Ψ (from 10^{-4} up to 1 sun) conditions. Each Ψ level was automatically calibrated by the Zahner station, through an integrated silicon-photodiode in closed-loop active feedback correction. Impedance spectroscopy measurements (IS) were carried out under voltage bias from 0V (short-circuit (J_{SC})) to *V*oc (open-circuit) at different illumination Ψ, ensuring an initial stabilization of 1 min at each condition, within a 1 MHz - 100 mHz frequency (ω) range at 6 points per decade and 3 points per period averaging (signal-to-noise ratio). For the voltage perturbation, an AC sinusoidal signal (V_{AC}) with 15 mV amplitude is applied superposed to the DC biasing point (V_{DC}). A cooling plate with an integrated Peltier unit was used for temperature control at 25 °C standard test conditions. The stabilized V_{OC} and J_{SC}, at each illumination Ψ, were recorded for SunVoc analysis. EQE/IPCE measurements were taken at 0V bias, in the photosensitive range (300-840 nm) of the perovskite absorber, with a15-nm step resolution, using a 3x3 mm mask.

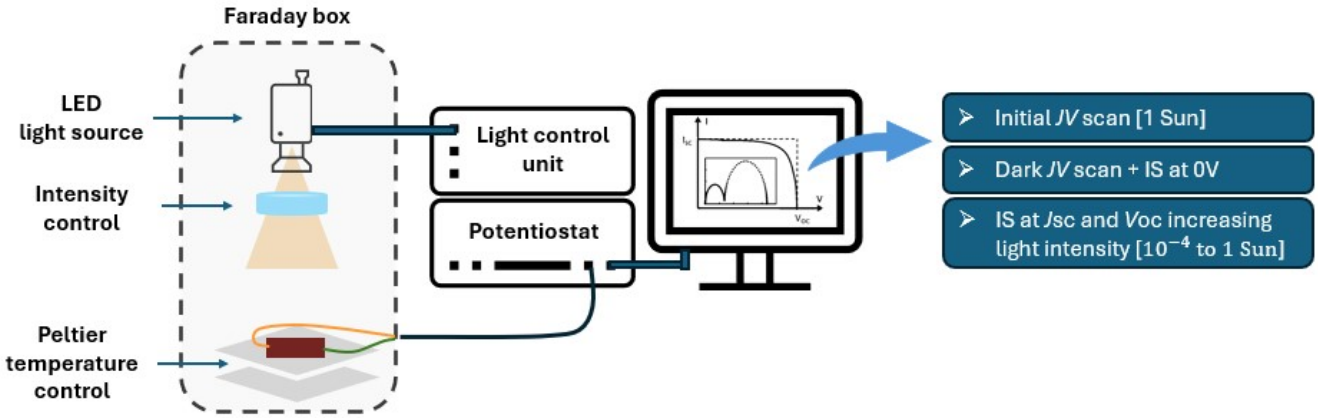

Figure S1 Characterization setup illustration (left) for integrated J-V/IS/SunsVoc measurement protocol, along with summary of key steps combined with DD simulations for the results analysis (right), applied to the selected PSCs.

We provide additional crystallographic (X-ray diffraction (XRD)), optical absorbance (UV-Visible), external quantum efficiency (EQE) and *J–V* curves at 1 sun, comparing the initial (fresh) and final (after *J-V*/IS protocol) quality in top performing cells (see next section S3, in **Figs. S3.5** to **S3.8)**, to attest for PK films quality and the performance stability in selected PSC architecture.

Drift-diffusion simulations

The open source *Driftfusion* code developed by Calado, et al. was used to simulate *J-V*/IS measurements, using a one-dimensional (finite difference) model, assuming lateral homogeneity and isotropic conditions [1]. An equivalent device composed of three main layers was defined in the model, respectively corresponding to: the perovskite absorber (450 nm), sandwiched between two thin selective transport layers (ETL and HTL, 30 nm each). The main input properties defined for each layer, as well as interfacial and boundary conditions, are summarized in detail in **Table S1**.

The main opto-electric properties studied in the simulations were the electron and hole mobility (μ_{PK}), in the ambipolar perovskite absorber, the free carrier lifetime for trap-mediated Shockley-Read-Hall recombination (τ_{PK}^{SRH}), ionic charge conductivity (by varying N_{ion} at fixed values for μ_{ion}), as well as the energetic bands offsets for majority carriers of the selective contacts at the PK/CTL interface (varying ΔCB for the ETL and ΔVB for the HTL). Two species of mobile ions are included within the ionic-electronic conductive properties of the perovskite layer at the same concentration (N_{ion}) for analysis simplicity. In this case, cations and anions with slow mobility (μ_{ion}) correspond most likely to iodine vacancies ($V_I^{\bullet}$) and A-site vacancies, as for the small organic molecule methylammonium ($V_{MA}^{'}$), as predicted by first principle calculations [2,3].

Metal contacts are treated as ohmic and aligned with the Fermi levels of the charge transport layers, following a common approximation in DD modelling. Although the work function of Gold (Au) (5.1–5.3 eV) differs from that of n-type SnO_2 (4.2-4.5 eV, with an electron affinity of 4.0-4.5 eV) under ideal vacuum-level alignment, higher doping concentration, and interfacial effects such as dipoles and Fermi level pinning can significantly modify the effective band alignment.

A perfect alignment was assumed in the selective contacts, between the Fermi level (E_F) of the transport layer (ETL/HTL) and the adjacent electrode work function (ϕ). Thus, the built-in potential (V_{bi}) that corresponds to the difference in electrodes work functions ($\Delta\phi$), was adjusted in line with the ΔCB and ΔVB set as inputs for the calculations at contact equilibrium conditions. The magnitudes for the input parameters in *Driftfusion* were defined considering as a reference the values used in literature for similar PSC architectures [4–6].

Table S1: Input parameters used in this work for DD simulations using *Driftfusion* open-source code [1]

Layer type	**Contact**	**Layer**	**Interface**	**Active**	**Interface**	**Layer**	**Contact**
	Anode	HTL		Perovskite		ETL	Cathode
Thickness (cm)		3×10^{-6}	1×10^{-6}	4.5×10^{-5}	1×10^{-6}	3×10^{-6}	
Electron affinity χ_e (eV)		-2.8		-3.8		-3.8 - (ΔCB offset)*	
Ionization potential χ_h (eV)		-5.4+(ΔVB offset)*		-5.4		-6.4	
Work function ϕ (eV)	$E_{F\ HTL}$†						$E_{F\ ETL}$†
Equilibrium Fermi energy E_F (eV)		χ_h + 0.1		-4.6		χ_e - 0.1	
Trap energy level (eV)		$E_{F\ HTL}$ + 0.05**		-4.6 (E_g/2)		$E_{F\ ETL}$ - 0.05**	
Effective density of states Nc/Nv (cm^{-3})		10^{19}		10^{19}		10^{19}	
Equilibrium concentration of cations (cm^{-3})				10^{15}-10^{19}			
Equilibrium concentration of anions (cm^{-3})				10^{15}-10^{19}			
Maximum concentration of cations (cm^{-3})				$1.21x10^{22}$			
Maximum concentration of anions (cm^{-3})				$1.21x10^{22}$			
Charge carrier mobility of electrons ($cm^2V^{-1}s^{-1}$)		5×10^{-2}	0.2-20	0.2-20	0.2-20	5×10^{-2}	
Charge carrier mobility of holes ($cm^2V^{-1}s^{-1}$)		5×10^{-2}	0.2-20	0.2-20	0.2-20	5×10^{-2}	
Charge carrier mobility of cations ($cm^2V^{-1}s^{-1}$)		0	0	10^{-9}	0	0	
Charge carrier mobility of anions ($cm^2V^{-1}s^{-1}$)		0	0	10^{-11}	0	0	
Dielectric constant		4	23	23	23	6	
Generation rate ($cm^{-3}\ s^{-1}$) at 1 sun equivalent (Gφ)		0	0	2.64×10^{21}	0	0	
Band-to-band recombination rate ($s^{-1}cm^3$)		1×10^{-12}	0	3.6×10^{-12}	0	3.2×10^{-11}	
Shockley-Read-Hall lifetime for electrons (s)		10^{-6}		10^{-6}-10^{-8}		10^{-6}	
Shockley-Read-Hall lifetime for holes (s)		10^{-6}		10^{-6}-10^{-8}		10^{-6}	
Recombination velocity for electrons ($cm\cdot s^{-1}$)	10^7		1		10^7		10^7
Recombination velocity for holes ($cm\cdot s^{-1}$)	10^7		10^7		1		10^7
Shunt resistance (Ωcm^2)	10^8						
Series resistance (Ωcm^2)	3						

* ΔCV (conduction band) or ΔVB (valence band) for band energy level of majority carriers. Positive Δ for ETL or HTL when offset goes into perovskite bandgap.

** Traps energy level defined 0.05eV below (above) ε_F for ETL (HTL) corresponding to shallow defects, while at mid gap for deep defects in the perovskite.

† Electrode work function (ϕ) assumed to be perfectly aligned to the fermi level (E_F) in equilibrium when put in contact with the respective CTL (ETL or HTL).

S2. IS principles, reported *RC* contributions and ECM transfer functions

Method description and main representations

The complex $Z(\omega)$ transfer function, as shown in **Equation S1**, corresponds to the linearized relation between the output current response $J(\omega t)$ to an input voltage $V(\omega t)$, both composed of a constant base (DC) and alternating sinusoidal (AC) signals (**Eq. S2 and S3**). The V_{AC} component has a small V_0 perturbation amplitude that when applied through the contact electrodes it induces the internal ΔE_F modulation within the device. Then, for every frequency ($\omega = 2\pi f$) point $Z(\omega)$ is composed by a modulus ($|Z(\omega)|$) and phase angle (Φ) corresponding to the J_{AC} delay with respect to the V_{AC} signal. As in main **Fig. 2**, common ways to represent the IS response are: (i) Nyquist Z' vs Z'' plots that typically display two or three characteristic semicircles for PSC or (ii) with their equivalent capacitance vs frequency Bode plot [7–10]. A physical interpretation of the frequency dependence of $Z(\omega)$ is modelled with the fits to the ECM (as depicted in the inset of **Fig. 2 (d)**), that represents the resistive paths (R_S, R_{HF} and R_{LF}) and capacitive components (CPE_{HF} and CPE_{LF}) related to charge dissipation and accumulation dynamics within the device.

$$Z(\omega) = \frac{V_0}{J_0} e^{-i\Phi(\omega)} = |Z(\omega)|(\cos(\Phi) - i\sin(\Phi)) = Z' - iZ'' \quad \text{(S1)}$$

$$V(\omega t) = V_{DC} + V_{AC} = V_{DC} + V_0 \sin(\omega t) \quad \text{(S2)}$$

$$J(\omega t) = J_{DC} + J_{AC} = J_{DC} + J_0 \sin(\omega t + \Phi) \quad \text{(S3)}$$

The capacitance Bode plots display an apparent capacitance, for the whole $Z(\omega)$ response, corresponding to the real part (C') of the equivalent complex capacitance (C^*), that is plotted as a function of ω (as in **Eq. S4**). For the characteristic IS response in selected ECM, each capacitance plateau corresponds to a characteristic $\tau = RC$ relaxation time. Nevertheless, more diverse models including inductive elements (see **Fig. S2**), or also with more elaborated arrangements, have been widely proposed in literature [7–9,11]. For instance, when inductive loops or hooks of negative capacitance arcs can appear in the Nyquist representation at intermediate and low frequencies.

$$C^*(\omega) = (i\omega Z)^{-1} = C'(\omega) - i\,C''(\omega) \quad \text{(S4)}$$

Frequency and time-domain relation

Gonzalez et al. showed the existence of a spectral connection, at any given illumination Ψ and voltage (V_{app}) bias applied, between the *J-V* resistive response in quasi steady-state $J(V_{app})$ for the time domain ($t \to \infty$) and the total resistance ($R_S + R_{HF} + R_{LF}$) in the IS response towards very small frequencies ($\omega \to 0$) as in **Eq. S5**, if causality and stability conditions are met [12]. In addition to standard *JV* analysis, the measure of *RC* elements in PSCs via IS can provide more deconvolved information regarding fast electrochemical processes and other slow kinetics that limit the current response. Therefore, by comparing the characteristic relaxation times (τ), multiple ionic-electronic contributions can be traced at different locations within the device [8,10,12].

$$R_T(\omega \to 0) = R_S + R_{HF} + R_{LF} = \left(\frac{\partial V}{\partial J}\right)_{t \to \infty} \quad \text{(S5)}$$

Resistive contributions

The use of combined ECM models with standard DD tools [1,11,13–16], or the derivation of simplified analytical expressions as from reduced order Surface Polarization Models (SPMs) [17–20], has allowed a better correlation between IS and *J-V* analysis in PSCs. By evaluating the device response at different operating conditions, multiple resistive elements limiting the output current have been identified, such as:

(i) The series resistance (R_S), corresponding to ohmic losses of the contacts.

(ii) Parasitic shunts resistance (R_{SH}), from leakage currents related to the device quality.

(iii) Charge transport resistance (R_{Tr}), as expressed in **Eq. S6** to **S8**, that depends on the ionic-electronic conductivity (σ) properties in the perovskite, as well as the additional layers and interfaces in the path of charge extraction.

$$R_{Tr}\, \alpha\, (\sigma)^{-1} \quad \text{(S6)}$$

$$\sigma_{ion} = q\, N_{ion}\, \mu_{ion} \quad \text{(S7)}$$

$$\sigma_{elec} = q\, (n_e \mu_e + n_h \mu_h) \quad \text{(S8)}$$

Overall, ensuring charge continuity with a total current resulting from the addition of individual flux densities of free carriers (electronic conductivity (σ_{elec})) and mobile charged particles (ionic conductivity (σ_{ion})) within the device.

(iv) Recombination resistance (R_{Rec}) in **Eq. S9**, where R_{00} is the pre-exponential factor, determined mostly by kinetic competition between radiative bi-molecular (band-to-band) and traps-assisted SRH mechanisms, can be roughly estimated from the slope in dark *J-V* scans in the region where recombination current (J_d) is dominant,i.e., low parasitic R_S and R_{SH} contribution-.

$$R_{rec} = \left(\frac{\partial J_d}{\partial V}\right)^{-1} = R_{00} \exp\left[-\frac{q\, V_{app}}{n_{id} k_B T}\right] \quad \text{(S9)}$$

The multiple contributions, as defined in the DD simulation tool used here, are accounted via the Poisson-Nernst-Planck equations and Maxwell-Ampere law for displacement field currents, along with the Poisson's equation defining space charge and electrostatic potential distribution using the Blakemore's approximation to Fermi-Dirac statistics [1,21].

Capacitive contributions

Multiple capacitive sources have been studied in literature to explain the polarization measured on IS for classical silicon cells, thin-film, organic and lately PSC, both when increasing illumination at J_{SC} and/or V_{OC} bias [7,9,13,22–28].

(i) First, the classical capacitance arising from the formation of space-charged regions (C_{dl}) at the junction between two semiconductors when put in contact at equilibrium using a parallel plate capacitor approximation *(***Eq. S10***)*. For which, the width (w_D) of the depleted zone will depend on the applied voltage bias and of a background doping density N as defined by a local charge density profile. For instance, in the case of a one-sided (abrupt interface) with uniform charge density over a surface area (A)*,*

$$C_{dl} = \frac{\varepsilon_0 \varepsilon_r A}{w_D} \alpha \sqrt{\frac{\varepsilon_0 \varepsilon_r N}{(V_{bi} - V_{DC})}} \quad \text{(S10)}$$

where ε_0 and ε_r correspond to a constat permittivity of free space and the relative to the semiconductor, respectively.

(ii) When reducing V_{DC} towards reverse bias, the space-charged region extends into the total thickness ($w_D = d$) of the semiconductor fully depleted and the C_{dl} saturates towards its geometric capacitance (C_{geo}). The total geometric capacitance for a PSC architecture (C_{geo}^{T}) will correspond then to the equivalent of the parallel multilayer stack configuration (**Eq. S11**) dominated by the thicker material corresponding to the PK layer (d_{PK}) [10,13].

$$C_{geo}^{T} = \left(\frac{1}{C_{geo,\ HTL}} + \frac{1}{C_{geo,\ PK}} + \frac{1}{C_{geo,\ ETL}} \right)^{-1} \leq \frac{\varepsilon_0 \varepsilon_r^{PK}}{d_{PK}} \quad \text{(S11)}$$

(iii) In other hand, the variation of minority carriers density, generally denominated here as n (n_e^P fore$^-$ in a p-type or n_h^n for h^+ in a p-type)), within a semiconductors during the modulation of its electrochemical potential (E_{F_n}) yields in a capacitance of chemical nature (C_μ, in **Eq. S12**) [29].

$$C_\mu = q^2 d \frac{\partial n}{\partial E_{F_n}} \approx q^2 d \frac{dn}{dV} \quad \text{(S12)}$$

(iv) In p-n junctions, with the increase in ΔE_F at higher forward voltage bias the variation in J_d can introduce a sort of chemical capacitance from charge injection and diffusion (C_{diff}, in **Eq. S13**). The magnitude of C_{diff} at a given Z(ω) should increase exponentially under applied forward voltage bias (injected charge accumulation) and it depends on the diffusion lengths (L_e, L_p) and effective recombination lifetimes of electrons (τ_n, τ_p) and holes, respectively. PSCs having an intrinsic PK absorber layer, do not meet the standard C_{diff} definition, but it has been shown that non-ideal energetic levels alignment

at the PK/CTL interfaces can induced charge imbalances, making dominant SRH recombination to be determined by local minority carrier densities [4].

$$C_{diff}\,\alpha\, Im\left[\frac{1}{\omega}\left(\frac{L_e}{\tau_e\sqrt{1+i\omega\tau_e}}+\frac{L_p}{\tau_n\sqrt{1+i\omega\tau_h}}\right)\exp\left[\frac{q\,V_{DC}}{mk_BT}\right]\right] \quad \text{(S13)}$$

(v) Moreover, SRH kinetics can induce an additional chemical capacitance (C_t, in **Eq. S14**) related to the intermediate trapping-detrapping of carriers, defined by the emission rate ($1/\tau_n$) of defect-states within the bandgap at a concentration N_t, and an occupation probability ($\bar{f}_t$) defined by their trap energy level position with respect to E_{F_n} [22].

$$C_t = \frac{q^2\,N_t\,d}{k_BT}\,\bar{f}_t(1-\bar{f}_t) \quad \text{(S14)}$$

Nevertheless, within the DD simulation model used here, it is assumed trapping-detrapping to be fast enough to be out of the simulated timescales, and therefore it does not include trapped carriers in the Poisson' equation [1].

To explain the capacitive built-up observed experimentally towards low frequencies (C_{LF} in the selected ECM), in short-circuit or open-circuit conditions and under increasing illumination, alternative surface polarization models with slow kinetics (τ_{kin}) have been proposed in literature.

(i) First, as additional accumulation of electronic charges, resulting in the building of a surface capacitance (C_s, in **Eq. S15**) at the PK/CTL interfaces that depends on the PK bulk thickness and indirectly defines its electronic charge density (n_{bulk}) [26,27].

$$C_s = q\frac{dn_s}{dV}\,\alpha\,\sqrt{n_{bulk}}\exp\left[\frac{q\,V_{DC}}{2\,k_BT}\right] \quad \text{(S15)}$$

(ii) Secondly, through ion interfacial charge accumulation (ΔC_{ion}, in **Eq. S16**) within a diffuse double layer with a Debye length ($l_{D_{ion}}$) directly proportional to N_{ion} [28].

$$\Delta C_{ion} = \frac{\varepsilon_r\varepsilon_0}{l_{D_{ion}}}\alpha\,\sqrt{\frac{N_{ion}}{T}} \quad \text{(S16)}$$

(iii) Ravinshakar et al. proposed a combined model of slow ionic-electronic accumulation as the origin of the polarization, from the perspective of a delayed response in the internal voltage of the diode (V_{int}, in **Eq. S17**) to any externally applied bias (V). From which,

they identified that the C_{LF} polarization as function V_{OC} under increasing illumination can be described by an exponential activation as in main **Eq. 4** [30].

$$\frac{dV_{int}}{dt} = \frac{V_{int} - (V - V_{bi})}{\tau_{kin}} \quad \text{(S17)}$$

(iv) Furthermore, Ghahremanirad, et al. showed how exotic inductive loops and negative capacitance components, often observed at low frequencies, are physically explained by slow ionic-electronic dynamics with a surface polarization model [20]. Likewise, Alvarez et al. found a correlation between negative capacitance features and inverted hysteresis in dynamic *J-V* scans (lower PCE in reverse direction than forward) [31].

In other hand, Jacobs et al. argued that instead of interfacial-only mixed ionic-electronic charge confinement (denote here as $C_Q(\omega)$), which hardly could explain the large C_{LF} magnitudes of up to 1mF/cm^2, a significant out-of-phase Im(Z) component of the IS response can be added up to the observed polarization (**Eq. S18**) [11].

$$C_{LF}(\omega) = C_Q(\omega) + A_R(\omega) \quad \text{(S18)}$$

Specifically, they demonstrated through DD simulations how the presence of slow mobile ions, in a sufficient N_{ion} that screens the internal field, can modulate and induce a significant phase-delayed recombination (A_R, in **Eq. S19**), affecting the collection of photogenerated carriers.

$$A_R = \frac{\tau_{kin} R_{\tau_{kin}}}{1 + (\omega\tau_{kin})^2} \quad \text{(S19)}$$

Then, a positive $A_R > 0$ contribution (or a negative $A_R < 0$) will appear when there is a net reduction in recombination currents giving a net resistance variation $R_{\tau_{kin}} > 0$ (or with $R_{\tau_{kin}} < 0$) over the time of the slow V_{int} relaxation (see the contributions to total C_{LF} from DD simulated IS, in section S4 **Figs. S4.9** to **S4.11**). Such model can explain then the large capacitive polarization at low frequencies under increasing illumination and/or forward voltage bias via increased ions-mediated phase-delayed recombination (when $A_R > 0$) or even negative capacitance values (when $A_R < 0$). Furthermore, Moia et al. showed though a transistor-based circuital model how ionic redistribution can tune (ionic-gate) the PK/CTL interfacial misalignment in energy levels, controlling free carriers' injection and recombination [16].

Equivalent circuit model (ECM), transfer function equations

Non-linear least squares fittings were used for experimental and DD simulated IS measurements, where the general transfer function $Z(\omega)$ for the simplified ECM selected in this study (as depicted in **Fig. S2 (a)**) can be described with the set of **Eq. S20 - 21**.

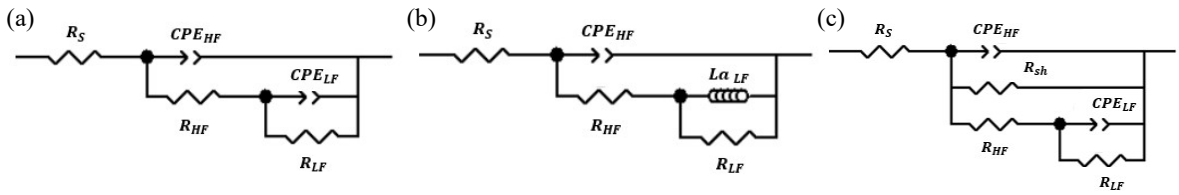

Figure S2 Simple equivalent circuit models, typically used for fittings of IS measurements, consisting of a series resistance R_S connected to two main *RC* Voigt elements in ladder configuration, where: (a) capacitive components at high (HF) and low frequency (LF) are modeled using constant phase elements -*CPE*-. (b) If the CPE_{LF} is replaced by a classical inductor to model loops or hook effects on IS arcs towards LF. (c) Additional shunt resistance (R_{SH}) element in parallel to the main circuit, to represent the parasitic influence of leakage currents in the general resistive response.

As a reference case, of ideal cole-cole *RC* relaxation, both at high (HF) and low (LF) frequency, using a Laplace transformation ($s = i\omega$):

$$Z(s) = R_S + \left[C_{HF}.s + \frac{1}{R_{HF} + Z_{LF}}\right]^{-1} \quad (S20)$$

$$Z_{LF} = \left[C_{LF}.s + \frac{1}{R_{LF}}\right]^{-1} \quad (S21)$$

Constant phase elements (*CPEs*) contain a dimensionless exponent (α) and an admittance constant ($Q_0, in\ Fcm^{-2}s^{\alpha-1}\ units$), as presented in equation S22 that denotes the characteristic transfer function (Z_{CPE}). First, the ideal capacitor elements (C) with $\alpha = 1$, were replaced by *CPE*s to account for non-ideal effects in bulk materials and interfaces (e.g., inhomogeneities inducing slight variations in local opto-electric properties), that induce a dispersion in the two characteristic *RC* time constants of PSCs at high (HF) and low (LF) frequency, respectively [32,33]. *CPE*s with $0.5 < \alpha < 1$ values are still indicative of a dominantly capacitive nature.

$$Z_{CPE}(s) = \frac{1}{s^{\alpha}Q_0} \quad (S22)$$

Moreover, the effective capacitance (C_{eff}) for each *CPE* is calculated as follows [34],

$$C_{eff} = \left(R^{(1-\alpha)}Q_0\right)^{\frac{1}{\alpha}} \quad (S23)$$

Then, the overall equivalent circuit model (ECM) transfer function (Z) as presented in **Fig. S2 (a)** corresponds to,

$$Z(s) = R_S + \left[Q_{0,\,HF} .s^{\alpha,HF} + \frac{1}{R_{HF} + Z_{LF}(s)} \right]^{-1} \quad (S24)$$

$$Z_{LF}(s) = \left[Q_{0,\,LF} .s^{\alpha,LF} + \frac{1}{R_{LF}} \right]^{-1} \quad (S25)$$

In this study, we did not observe any IS fits displaying $\alpha < 0.7$, see SI tables S4.1 and S4.2, which suggest a dominant capacitive nature for the *CPE* elements used. Although we provide other drift-diffusion simulations with inductive features at LF, see **Fig. S4.10 (c-d)**. For those cases, an alternative ECM was used, including a CPE_{LF} with $\alpha = -1$ accounting for an ideal inductor, as shown in equation S26 and the **Fig. S2 (b)**.

$$Z_{LF}(s) = \left[\frac{1}{L_a.s} + \frac{1}{R_{LF}} \right]^{-1} \quad (S26)$$

If additional losses from parasitic leakage currents are now included as a direct physical element, i.e., with the shunt resistance (R_{sh}) in parallel to the main ECM ladder as depicted in **Fig. S2 (c)**, the modifications to the impedance Z(s) characteristic transfer function yield in [33],

$$Z(s) = R_S + \left[C_{HF} .s + \frac{1}{R_{HF} + Z_{LF}} + \frac{1}{R_{SH}} \right]^{-1} \quad (S27)$$

S3. *J-V*/SunsVoc characterization and complementary results on PSCs quality

Performance parameters at 1 sun (AM1.5G) equivalent illumination

For experimental results, presented as black dots distributions in main **Fig. 2**,

Table S3.1: Performance parameter, mean values and 95% confidence intervals, extracted from fittings to 1-diode model, for *J-V* S cans at 1 sun illumination, using an Oriel solar simulator and a Silicon + KG5 reference cell.

Scan	J_{SC} (mA.cm^{-2})	V_{OC} (V)	FF (%)	PCE (%)	R_S (Ω.cm^{-2})	R_{Sh} (Ω.cm^{-2}) •10^{+3}	J_0 (A.cm^{-2}) •10^{-11}	n_{id}
FW	18.67 ± 0.39	1.11 ± 0.02	70.62 ± 5.36	14.60 ± 1.20	4.29 ± 1.88	2.05 ± 0.59	334.93 ± 972.55	2.57 ±0.71
RV	18.66 ± 0.39	1.12 ± 0.03	71.62 ± 4.74	15.02 ± 1.15	3.70 ± 1.59	1.76 ± 0.79	149.65 ±356.93	2.51 ± 0.63

Other performances reported in literature, for similar inverted PSC architectures,

Table S3.2: Summary of performance parameters and main layers compositions reported in literature for representative studies in similar inverted (p-i-n) PSC architectures.

Stack architecture	Area (cm^2)	V_{OC} (V)	J_{SC} ($mA.cm^{-2}$)	FF (%)	PCE (%)	[Source] (year)
ITO/PTAA/$Cs_{0.05}(FA_{0.92}MA_{0.08})_{0.95}Pb(I_{0.92}Br_{0.08})_3$/$C_{60}$/BCP/Cu	0.10	1.17	24.1	81.6	22.3	(2020) [35]
ITO/NiO_X/ MeO-2PACz/ $MAPbI_3$/C_{60}/BCP/Ag	0.10	1.12	22.3	80.2	19.9	(2021) [36]
ITO/PTAA/$Cs_{0.05}(FA_{0.92}MA_{0.08})_{0.95}Pb(I_{0.95}Br_{0.05})_3$/$C_{60}$/BCP/Ag	0.07	1.17	23.9	83.6	22.6	(2021) [37]
ITO/PTAA/$Cs_{0.05}(FA_{0.98}MA_{0.02})_{0.95}Pb(I_{0.98}Br_{0.02})_3$/$FcTc_2$/$C_{60}$/BCP/Ag	0.08	1.18	25.7	82.3	25	(2022) [38]
ITO/NiO_X/$Cs_{0.05}FA_{0.85}MA_{0.01}PbI_3$/3F-PEIA/PCBM/BCP/Ag	0.05	1.15	24.9	83.5	23.9	(2022) [39]
ITO/MeO-2PACz/$Rb_{0.05}Cs_{0.05}FA_{0.85}MA_{0.05}Pb(I_{0.95}Br_{0.05})_3$/ 3-APy/LiF/$C_{60}$/BCP/Ag	0.11	1.16	26.1	83.82	25.37	(2022) [40]
ITO/NiO_X/$Cs_{0.33}(FA_{0.85}MA_{0.15})_{0.67}Pb(I_{0.88}Br_{0.12})_3$/$PC_{61}BM$:$C_{60}$/ BCP:TTTS/Au	0.10	1.20	22.35	82.36	21.87	(2022) [41]
ITO/ NiO_X/Me-4PACz/$Cs_{0.2}FA_{0.8}Pb(I_{0.947}Br_{0.053})_3$/ LiF/$C_{60}$/BCP/Ag	0.13	1.14	24.1	79.40	21.8	(2023) [42]
ITO/Me-4PACz + PHA /$Cs_{0.05}(FA_{0.90}MA_{0.10})_{0.95}Pb(I_{0.80}Br_{0.20})_3$/PCl C_{60}/SnO_2/Ag	0.10	1.23	21.15	85.25	22.24	(2024) [43]
ITO/NiO_X/D4P/$Cs_{0.1}FA_{0.9}PbI_3$/C_{60}/BCP/Ag	0.05	1.17	25.61	85.1	25.57	(2024) [44]

PTAA (*poly[bis(4-phenyl)(2,4,6-trimethylphenyl)amine*) - BCP (*bathocuproine*)
$FcTc_2$ (*ferrocenyl-bis-thiophene-2-carboxylate*) - 3-APy (*3-(aminomethyl)pyridine*) – PHA (*6-Phosphonohexanoic acid*)
MeO-2PACz (*2-(3,6-dimethoxy-9H-carbazol-9-yl)ethyl]phosphonic acid*)
Me-4PACz (*[4-(3,6-dimethyl-9H-carbazol-9-yl)butyl]phosphonic acid*)
$PC_{61}BM$:C_{60} (*[6,6]-phenyl-C61-butyric acid methyl ester ($PC_{61}BM$) doped with C_{60} fullerene*)
BCP:TTTS (*bathocuproine (BCP) with additive 1,3,5-triazine-2,4,6-trithiol trisodium salt (TTTS)*

Dark *J-V* and SunsVoc measurements, recombination analysis with 1-diode model

Table S3.3: Main solar cell parameters, extracted from fits to 1-diode of dark *J-V* scans and SunsVoc measurements, as shown in main **Fig. 4 (a)**.

Scan	Fits from J_{SC}-V_{OC}		Dark *J-V* derivate	Fits from Dark *J-V*			
	J_0 ($mA.cm^{-2}$) •10^{-11}	n_{id}	Minimum $n_{id}(V)$	n_{id}	J_0 ($mA.cm^{-2}$) •10^{-11}	R_S ($\Omega.cm^{-2}$)	R_{SH} ($\Omega.cm^{-2}$) •10^{+8}
FW	150	2.0	1.9	2.1	238	10.31	1 (fixed as in DD)
RV			1.9	2.1	186	12.19	1 (fixed as in DD)

Table S3.4: SunsVoc, measured experimentally as J_{SC}-V_{OC} points, using the white LED (4300 K) light source of the Zahner workstation, under different light illumination intensities.

Light intensity Ψ (Suns)	V_{OC} (V)	J_{SC} ($mA.cm^{-2}$)
$1x10^{-4}$	0.62	$3.36\ x10^{-4}$
$3.5x10^{-4}$	0.69	$1.23x10^{-3}$

$1x10^{-3}$	0.75	$3.60\ x10^{-3}$
$3.5x10^{-3}$	0.81	$1.28\ x10^{-2}$
$1x10^{-2}$	0.87	$3.66\ x10^{-2}$
$3.5x10^{-2}$	1.01	$5.37x10^{-1}$
$1x10^{-1}$	1.07	1.54
$3.5x10^{-1}$	1.12	5.38
1	1.16	15.29

X-Ray Diffraction (XRD): crystallographic analysis of PK films stability

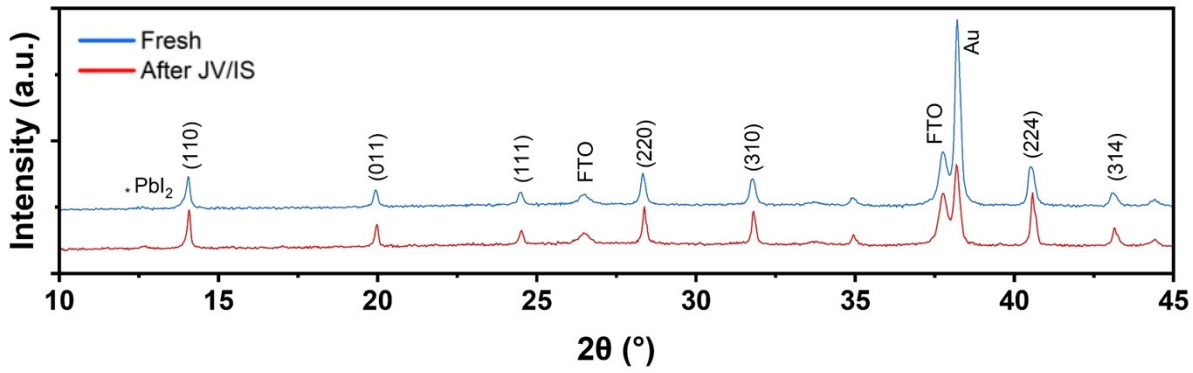

Figure S3.5 X-ray diffraction (XRD) of two PSC samples from selected architecture with (Au) opaque top contact electrode. Main XRD picks at 2θ angles of characteristic PK cubic (active) phase diffraction planes, with no additional degradation (***PbI_2 (12.6°)**) or phase transition signatures (**δ-phase (11°)**).

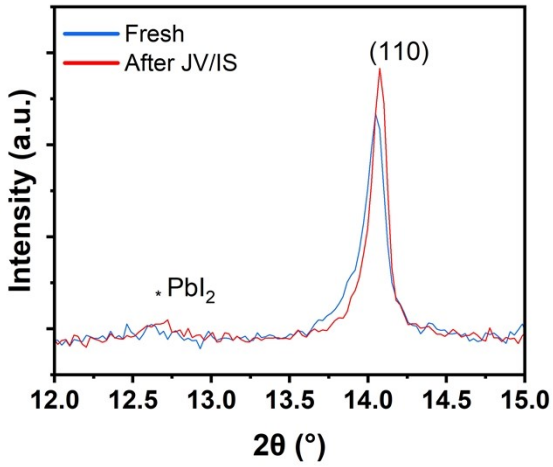

Figure S3.6 X-ray diffraction (XRD) of two PSC samples from selected architecture with (Au) opaque top contact electrode. Main XRD picks at 2θ angles of characteristic PK cubic (active) phase diffraction planes, with no additional degradation (***PbI_2 (12.6°)**) or phase transition signatures (**δ-phase (11°)**).

External quantum efficiency (EQE) and *J-V*: stability at 1 sun equivalent illumination

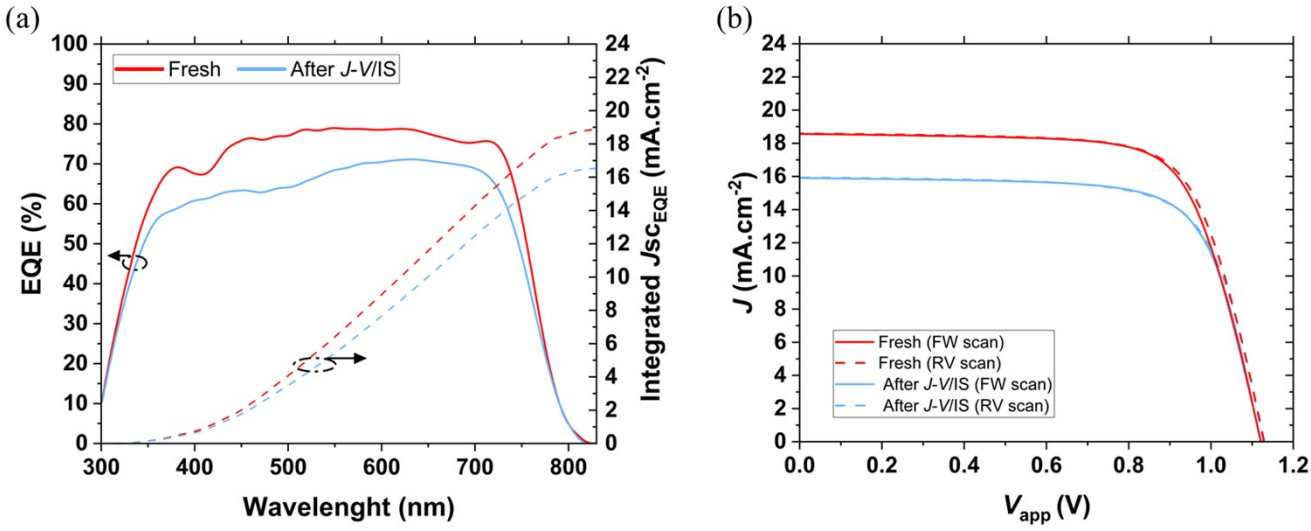

Figure S3.7 (a) External quantum efficiency (solid) and integrated current (dashed) at fixed 0V volage bias for a top performing cell, that is representative of the selected Au-opaque PSC architecture. (b) *J-V* scans in forward (solid) and reverse (dashed) scan direction at 30 mV/s and at 1 sun AM1.5G equivalent illumination using an Oriel solar simulator and a Silicon + KG5 reference cell. Comparison of PSC response in fresh (red) versus after application of the full characterization protocol (blue).

Absorbance UV-VIS: analysis of PK films' optical bandgap (E_g) stability

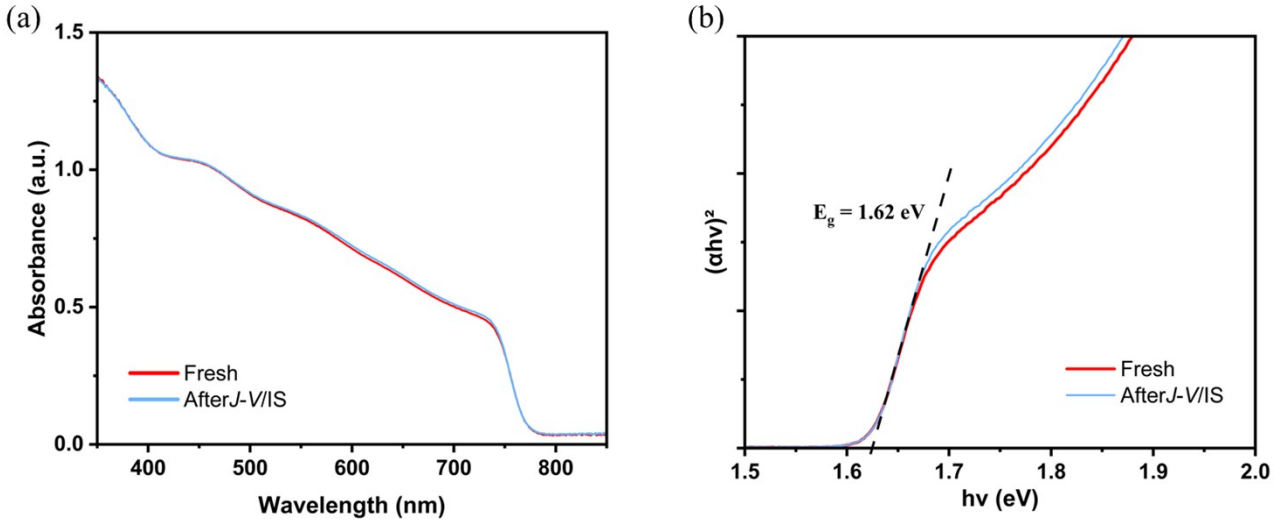

Figure S3.8 Optical absorption UV-VIS (a) measurements, with equivalent Tauc plot representation (b) for optical bandgap E_g estimation (black dashed line, at intercept in *hv* (eV)), for a top performing cell that is representative of the selected Au-opaque PSC architecture. Comparison of PSC response in fresh (red) versus after application of the full characterization protocol (blue).

S4: Complementary results on DD simulations

Ion accumulation profiles at different V_{bi} under the effect of increasing N_{ion}

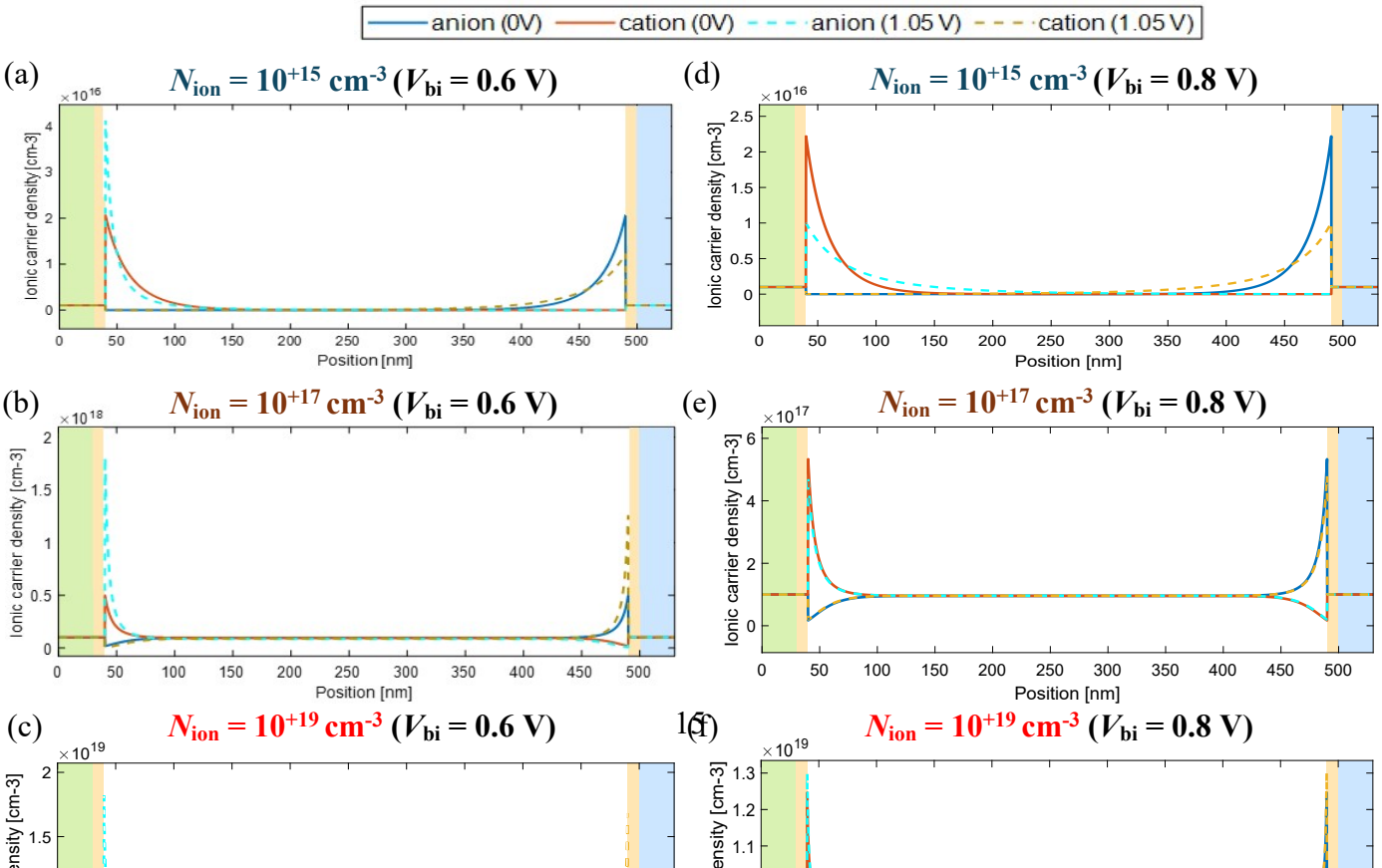

Figure S4.1 Cation and anion concentration profiles (confined in the PK) for initial N_{ion} set at: 10^{+15} cm^{-3} (a & d), 10^{+17} cm^{-3} (b & e) and 10^{+19} cm^{-3} (c & f). Plots under a resulting V_{bi} = 0.6 V (a-c) versus V_{bi} = 0.8 V (d-f). Equilibrium at 0V (solid lines) versus dark injection at V_{app} = 1.05V (dashed lines), with μ_{PK} = 0.2 cm^{2}V^{-1}s^{-1} and τ_{PK}^{SRH} = 1 μs.

Energy levels alignment under the effect of increasing N_{ion}

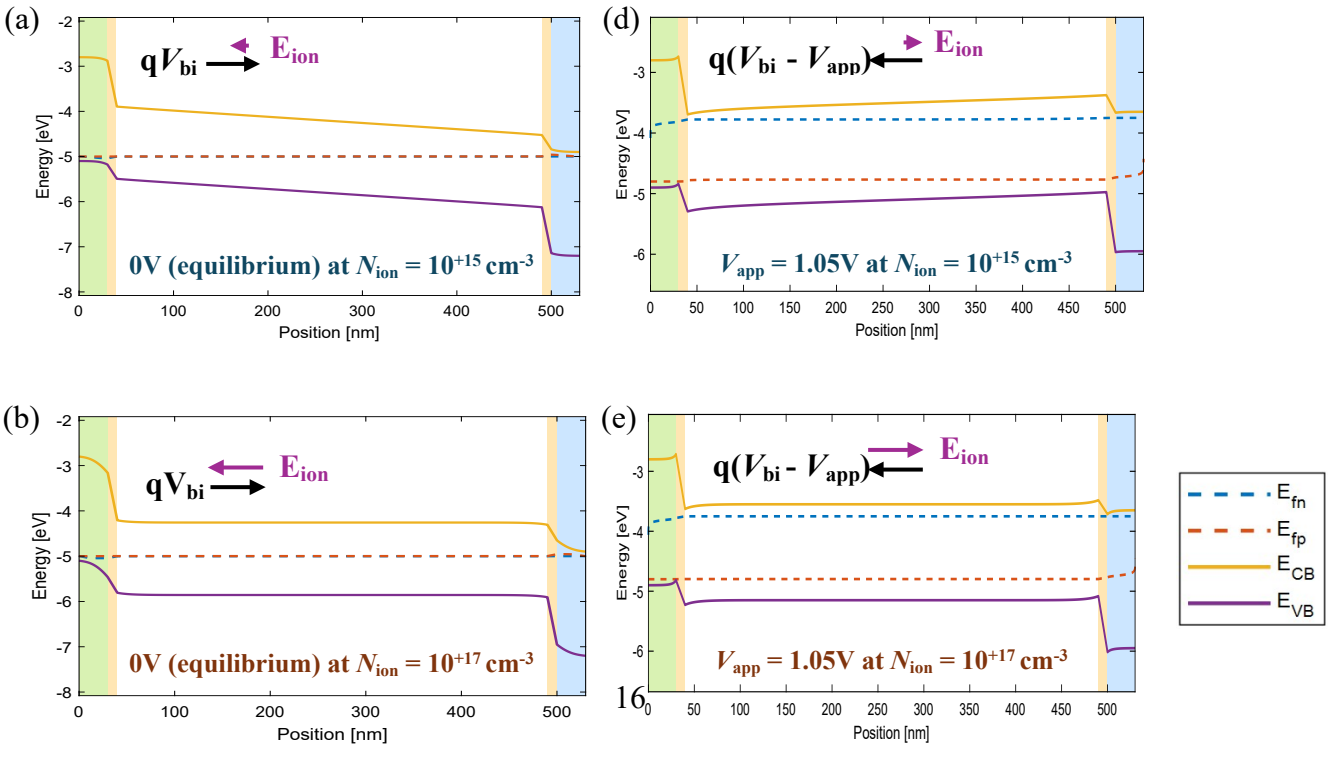

Figure S4.2 DD-simulated energetic alignments of PK/CTL when in contact at 0V (a-c) and at applied forward bias V_{app} = 1.05V in dark (d-f) under charge injection. Effect of field screening (E_{ion}) varying N_{ion} from 10^{+15} cm^{-3} (a & d), 10^{+17} cm^{-3} (b & e) and 10^{+19} cm^{-3} (c & f), under a resulting V_{bi} = 0.6 V. Conduction and valence bands (solid lines) and quasi-fermi levels of electrons and holes (dashed lines) throughout the 1D model of the PSC cross-section, with μ_{PK} = 0.2 $cm^2V^{-1}s^{-1}$ and τ_{PK}^{SRH} = 1 μs.

Effects of N_{ion} and energy barriers at PK/CTLs interfaces on recombination analysis

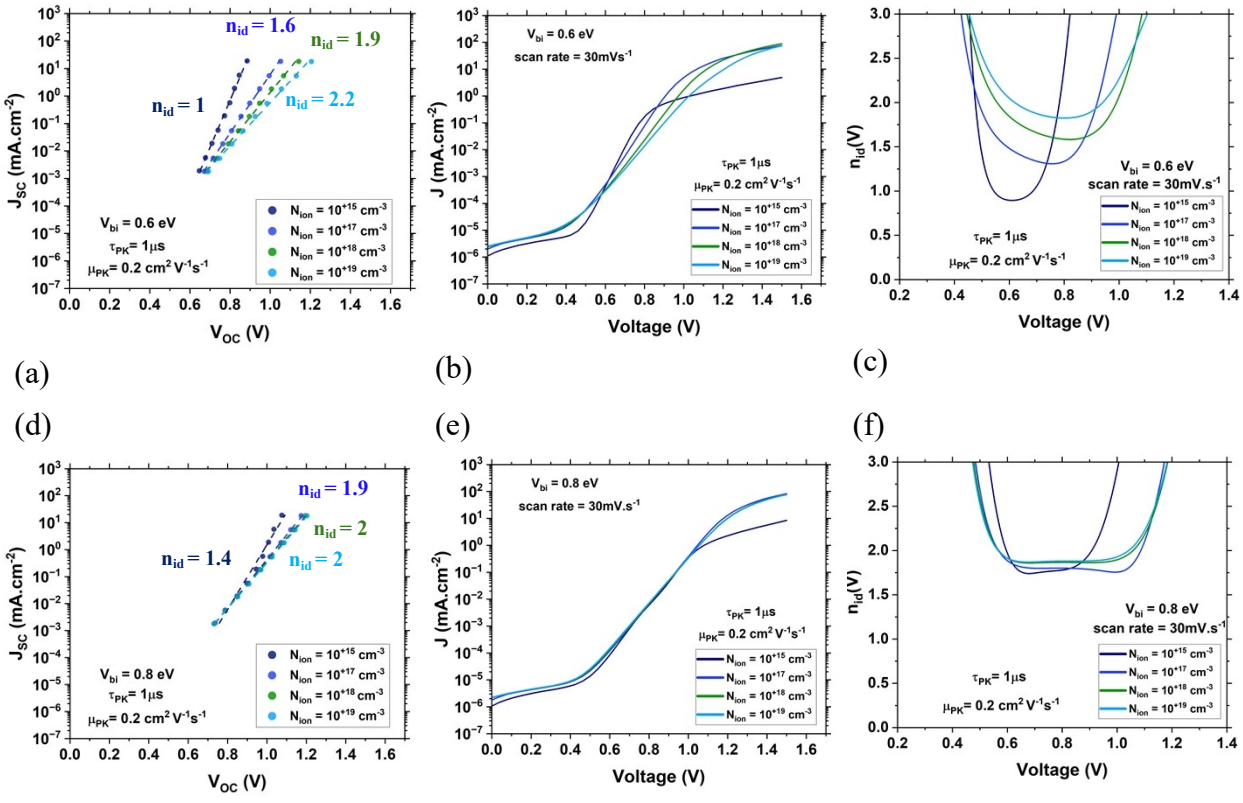

Figure S4.3 DD simulations of coupled effects under varying N_{ion} and ΔVB band offset at PK/HTL interface defining the V_{bi}. Dark *J-V* scans and *J*sc-*V*oc measurements for: a high ΔVB level of 500 meV at V_{bi} = 0.6 V (a-c) versus a reduced ΔVB level of 300 meV at V_{bi} = 0.8 V (a-f). *J*sc-*V*oc points with derived n_{id} using a 1-diode model (a & d). Dark *J-V* curves (b & e) include effects of parasitic shunts and R_S resistance saturation at low and high injection, respectively. Derived n_{id} from dark *J-V* curves presented separately in (c & f), showing a minimum $n_{id}(V)$ in the internal diode recombination (in between the rise in R_{SH} and R_S parasitic losses at low and high injection, respectively).

Free carrier's concentration of electrons and holes under the effect of increasing N_{ion}

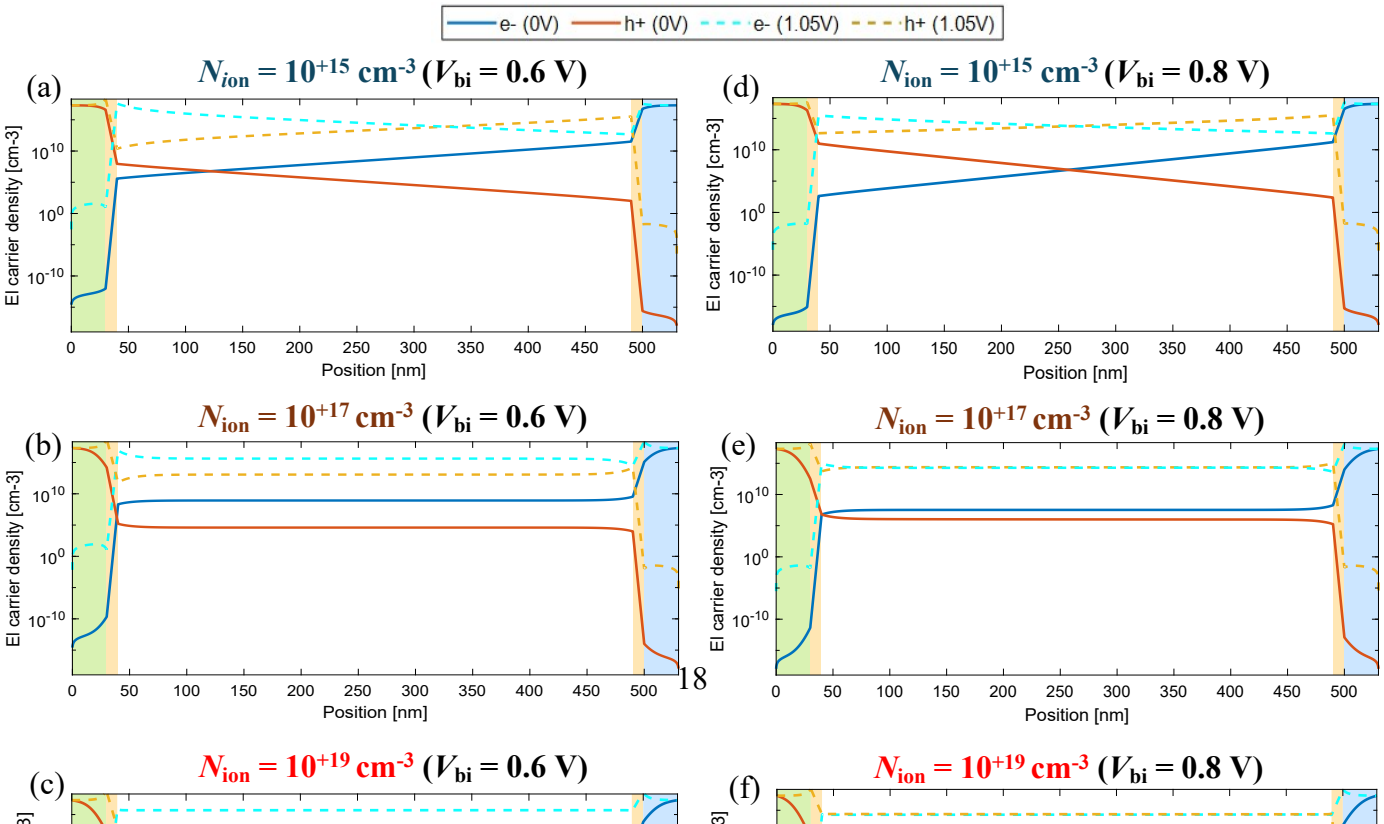

Figure S4.4 DD-simulated eh concentrations throughout the 1D model of the PSC cross-section, considering the effect of ΔVB/ΔCB band offsets an ionic screening with N_{ion} set at: 10^{+15} cm^{-3} (a & d), 10^{+17} cm^{-3} (b & e) and 10^{+19} cm^{-3} (c & f). Plots under a resulting V_{bi} = 0.6 V (a-c) versus V_{bi} = 0.8 V (d-f). Equilibrium condition at 0V (solid lines) versus under dark injection at V_{app} = 1.05V (dashed lines), with μ_{PK} = 0.2 cm^{2}V^{-1}s^{-1} and τ_{PK}^{SRH} = 1 μs.

DD simulated IS at J_{SC}: effect of V_{bi} at high vs low μ_{PK}

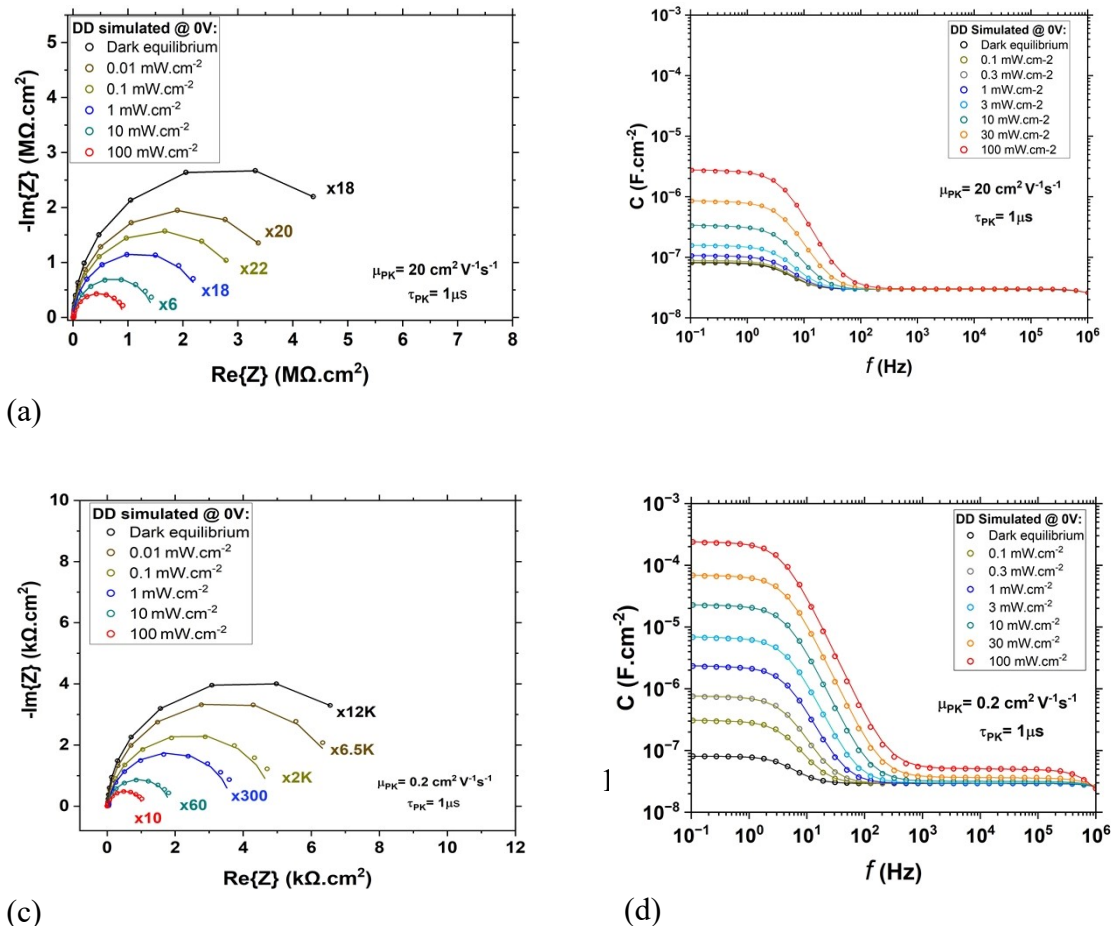

(f)

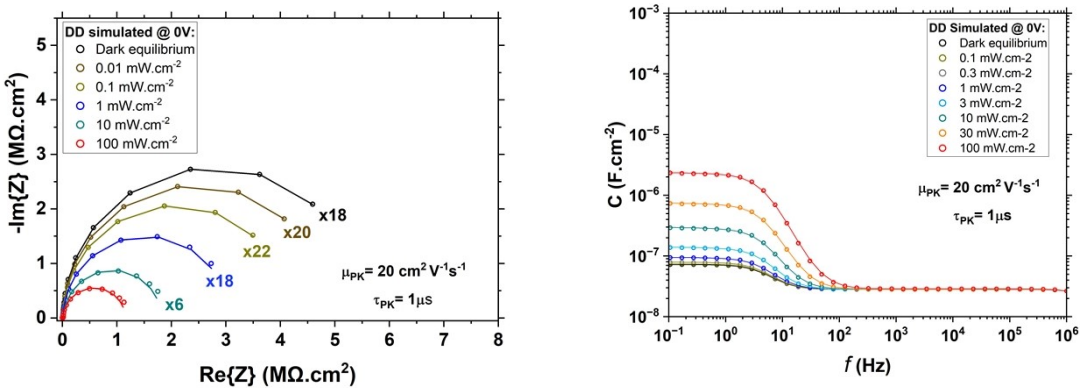

(e)

Figure S4.5 DD simulated IS at J_{sc} under increasing light illumination from 10^{-04} up to 1 sun equivalent. Nyquist representation in (a), (c) and (e), with two characteristic semi-circles observed. Capacitance vs frequency Bode plots in (b), (d), and (f), with HF plateau and additional polarization towards LF. DD simulated raw data (circles) data, plotted along with equivalent fit functions (solid lines) to selected ECM (as inset shown in **Fig. 2 (d)**). In addition to the parameters indicated at each plot and the ones presented on Table S1: N_{ion}= 10^{+18} cm^{-3}, (a-d) V_{bi}=0.6 V, (e-f) V_{bi}=0.8 V.

IS fits to selected ECM: R_{HF} and R_{LF} vs J_{SC}, equivalent effects of varying μ_{PK} and τ_{PK}^{SRH}

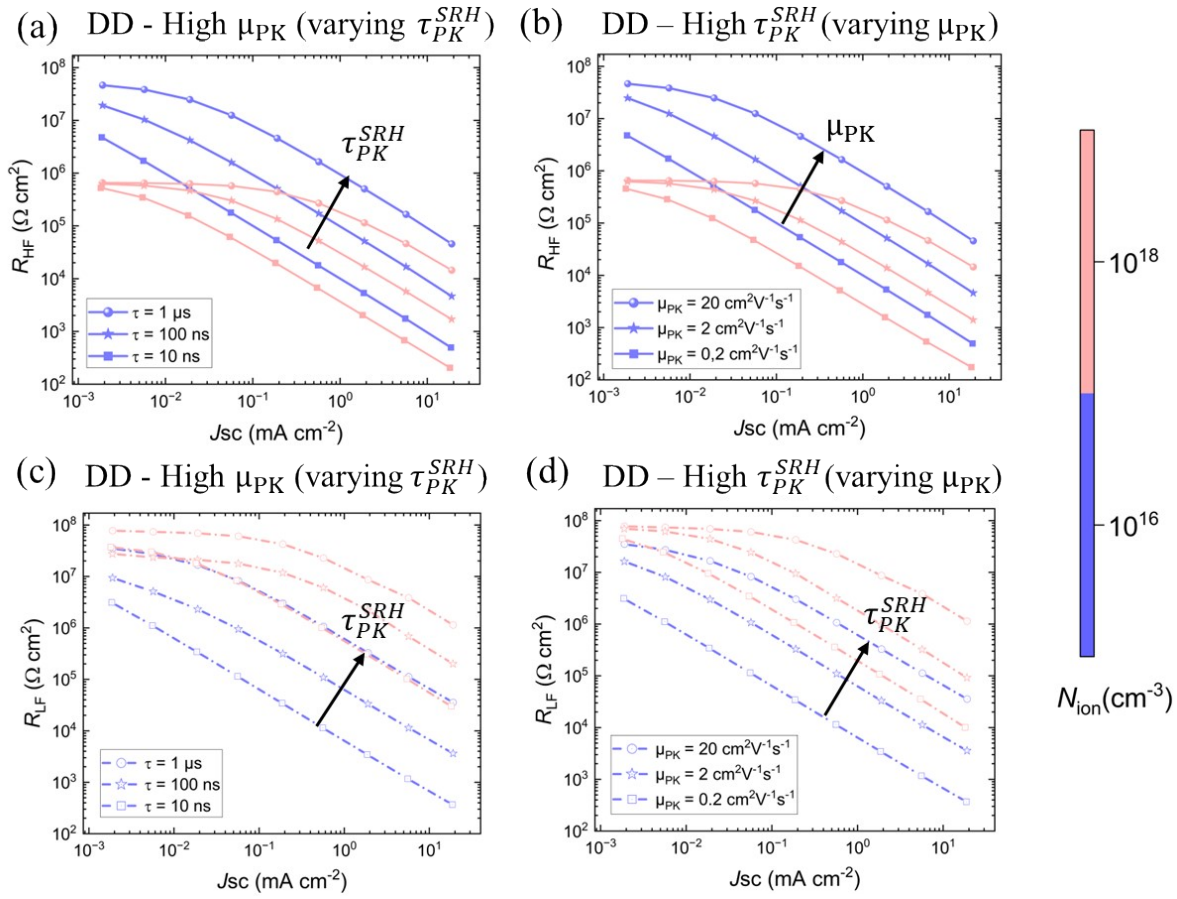

Figure S4.6 Simulated IS fits to selected ECM (as depicted in inset of main **Fig. 2 (d)**), with R_{HF} (a-b) and R_{LF} (c-d) as a function of J_{SC} under different light illumination intensities from 10^{-04} to 1 sun equivalent. The ion concentration varies in the steps of: $N_{ion} = [10^{16}, 10^{18}]$ cm^{-3} with fixed V_{bi}=0.6 V. Simulations varying effective eh recombination lifetime τ_{PK}^{SRH} in (a) and (c) at high μ_{PK}, compared to the variation of μ_{PK} in (b) and (d) at high τ_{PK}^{SRH}. Black arrows in direction that is indicative of rising magnitude and effects for the main varying parameter in each plot.

IS fits to selected ECM: R_{HF} and R_{LF} vs J_{SC} under low R_{SH} at different N_{ion}

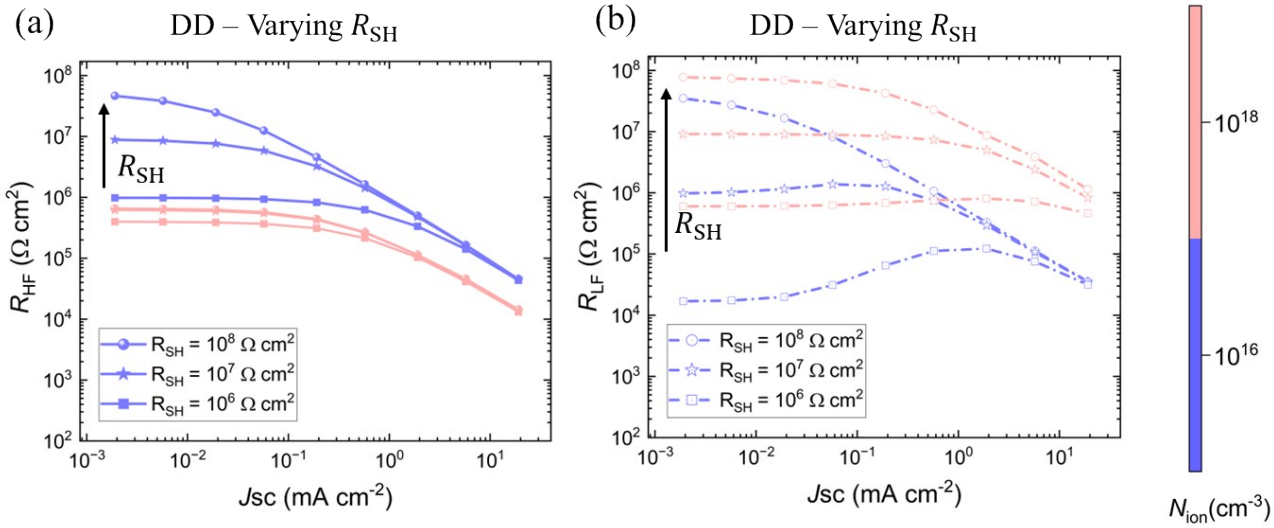

Figure S4.7 Simulated IS fits to selected ECM (as depicted in inset of main **Fig. 2 (d)**), with R_{HF} (a) and R_{LF} (b) as a function of J_{SC} under different light illumination intensities from 10^{-04} to 1 sun equivalent. The ion concentration varies in the steps of: $N_{ion} = [10^{16}, 10^{18}]$ cm^{-3} and $R_{SH} = [10^6, 10^7, 10^8]\ \Omega\ cm^2$; with fixed V_{bi}=0.6, μ_{PK}=20 $cm^2V^{-1}s^{-1}$ and τ^{SRH}_{PK}=1 μs. Black arrows in direction indicative of rising magnitude for the R_{SH}.

IS fits to selected ECM: C_{HF} and C_{LF} vs J_{SC} at different light illumination intensities

In PSCs, distinguishing the nature of the capacitance is challenging due to a strong overlap of characteristic relaxation times [7,8,13,45–47]. At high frequencies and low forward voltage bias, the high frequency capacitance C_{HF} primarily stems from electronic accumulation and dielectric displacement, governed by the multilayer permittivity and referred as the equivalent geometric capacitance $C^{T}_{geo} = \left\{ \sum_{i=layer} 1/C^{i}_{geo} \right\}^{-1}$ of the device. From simulations as in **Fig. S4.8 (b-c)**, C^{T}_{geo} follows closer the lowest layer geometric capacitance C^{i}_{geo}, corresponding to the expected for the thick perovskite layer $C_{geo,PK} \approx 4.5x10^{-08}\ F/cm^2$ [13,48]. For a low μ_{PK} = 0.2 cm^{2}V^{-1}s^{-1}, C_{HF} slightly increases at high J_{SC} values similar as in the experimental data in **Fig. S4.8 (a)**, unlike the flat response at high μ_{PK}. High N_{ion} can hinder electronic charge extraction from the PK layer and alter local charge accumulation. This leads to changes in the ion diffuse layer with Debye length $l_{D_{ion}}$ towards the interfaces, modifying charge density profiles. Consequently, the depletion width w_D (**as in Eq. S10**) and individual layer contributions to C^{T}_{geo} (**as in Eq. S11**) are affected.

The capacitance at low frequency C_{LF}, as shown in **Fig. S4.8 (d-f)**, increases with illumination consistent with ionic-modulated phase delay recombination (A_R), as proposed by Jacobs et al. [11].

DD simulations in **Fig. S4.8 (e-f)** confirm this behavior and show its sensitivity to variations in τ_{PK}^{SRH} and μ_{PK}. As previously shown [5], C_{LF} decreases with increasing $N_{ion} > 10^{17}$ cm^{-3} due to the screening of the built-in field. The increase in N_{ion} reduces $l_{D_{ion}}$, enhancing interfacial ion confinement and modulating A_R, leading to a decrease of C_{LF} with J_{SC}. While the IS response at the LF regime involves the same slow ionic-electronic nature for a constant $\tau_{LF} = R_{LF}C_{LF}$ towards high light illumination intensities (see **Fig. S4.13**), the HF regime involves distinct mechanisms that yield in a non-constant $\tau_{HF} = R_{HF}C_{HF}$: C_{HF} reflects mostly dielectric relaxation and R_{HF} is dominated by a combination of charge transport and recombination mechanisms.

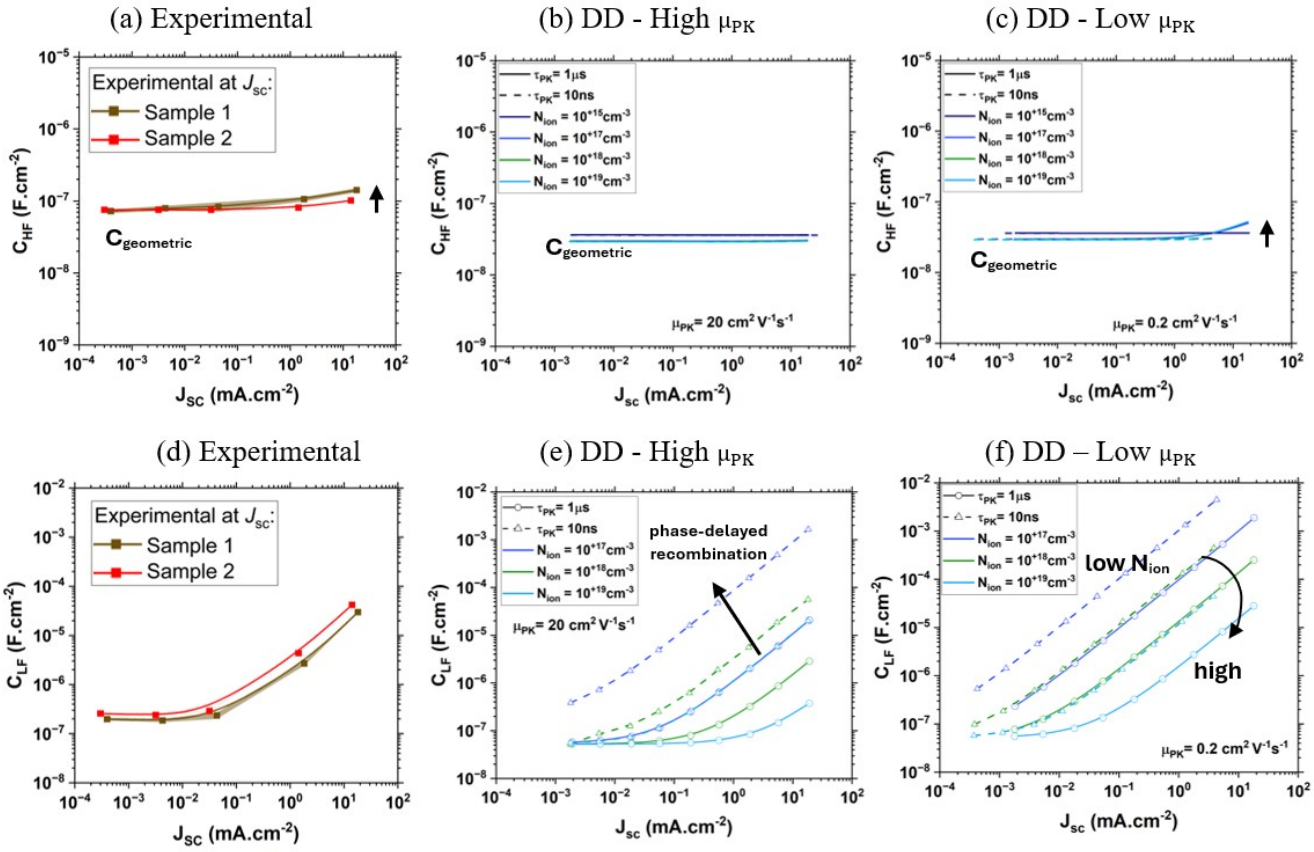

Figure S4.8 C_{HF} and C_{LF} vs J_{sc} under different light illuminations from 10^{-04} up to 1 sun equivalent, obtained from IS fits to selected ECM (as inset in main **Fig. 3 (a)**). Experimental (a & d) versus DD simulated (b-c & e-f) measurements, varying: $N_{ion} = [10^{15} - 10^{19}]$ cm^{-3}, $\mu_{PK}\,(cm^2V^{-1}s^{-1}) = \{0.2, 20\}$ and $\tau_{PK}^{SRH}(s) = \{10^{-06},\ 10^{-08}\}$. DD simulations at high (b & e) and low μ_{PK} (c & f), at fixed with V_{bi}=0.6 V. Black arrows in direction indicative of rising magnitude or effect related to the main varying parameters.

DD simulated IS at V_{OC}: effect of varying V_{bi} and μ_{PK} at high τ_{PK}^{SRH} – capacitive polarization towards LF

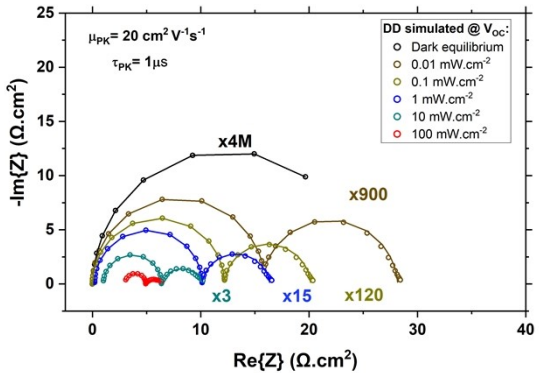

(a)

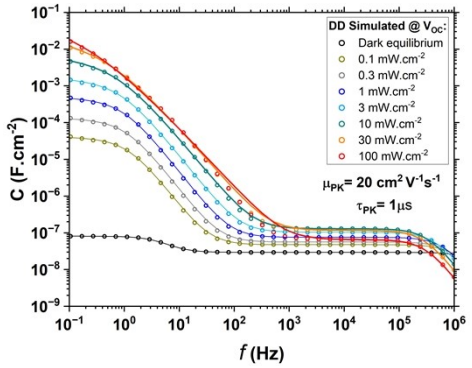

(b)

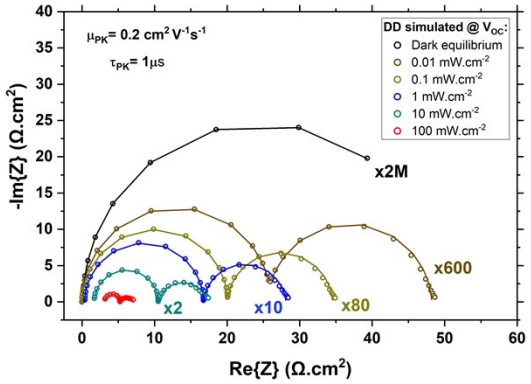

(c)

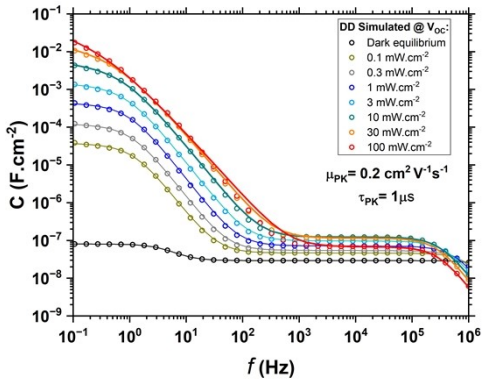

(d)

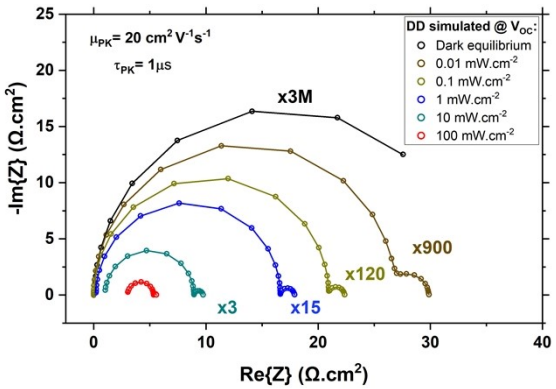

(e)

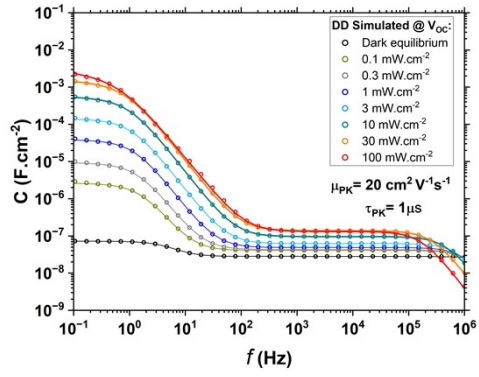

(f)

Figure S4.9 DD simulated IS at open-circuit (V_{OC}) under increasing light illumination from 10^{-04} up to 1 sun equivalent. Nyquist representation in (a), (c) and (e), with two characteristic semi-circles observed. Capacitance vs frequency Bode plots in (b), (d) and (f), with HF plateau and additional polarization towards LF. DD simulated raw data (circles) plotted along with fit functions (solid lines) to selected ECM (as inset shown in main **Fig. 2 (d)**). In addition to the parameters presented on Table S4.1: τ_{PK}^{SRH} = 1 μs and N_{ion}= 10^{+18} cm^{-3}, with (a-d) V_{bi}=0.6 V vs (e-f) V_{bi}=0.8 V. (a-b & e-f) μ_{PK} = 20 cm^{2}V^{-1}s^{-1} vs (c-d) μ_{PK} = 0.2 cm^{2}V^{-1}s^{-1}.

DD simulated IS at V_{OC}: effect of varying V_{bi} at reduced τ_{PK}^{SRH} – Inductive effects at LF

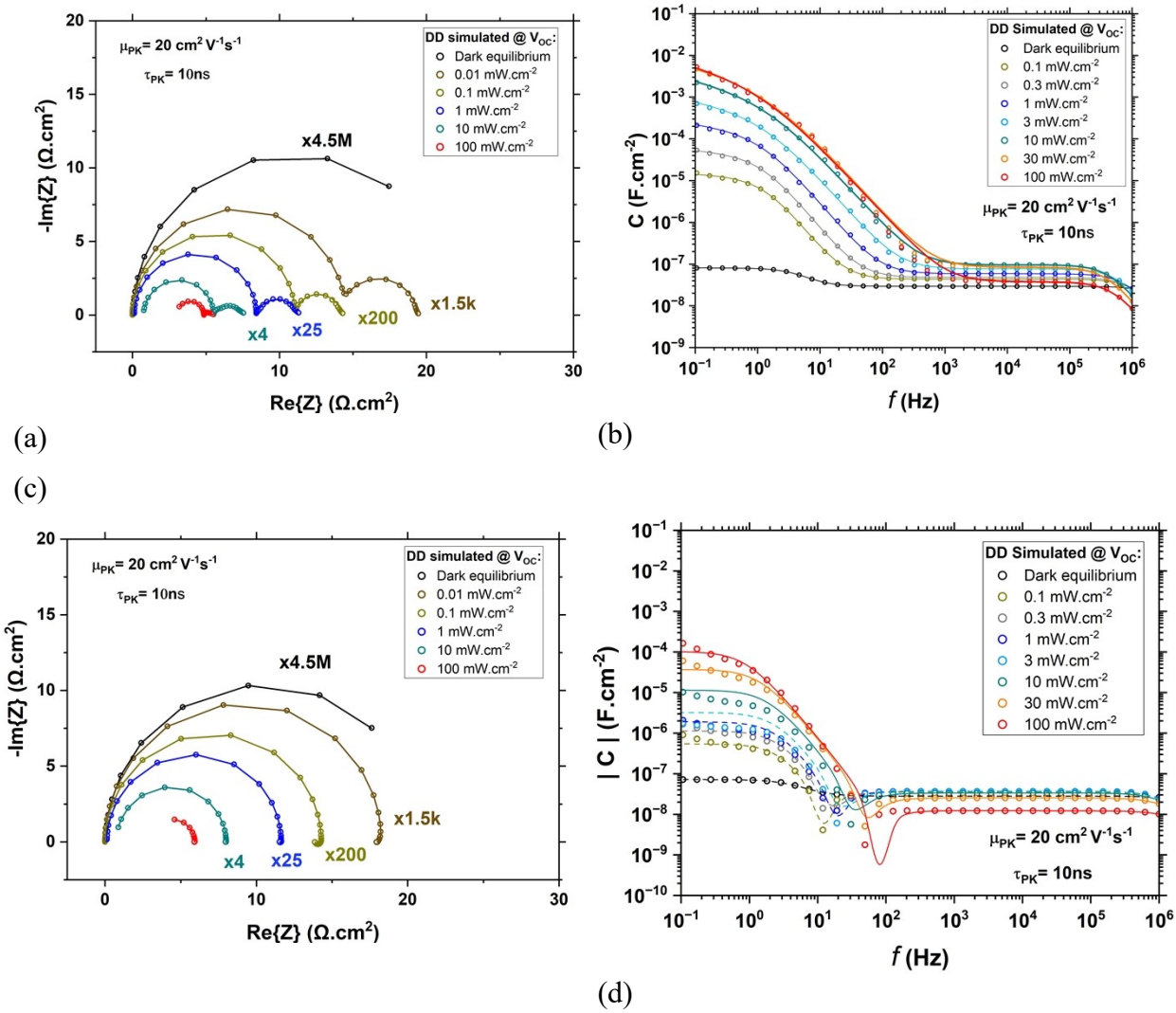

Figure S4.10 DD simulated IS in dark equilibrium and open-circuit (V_{OC}) under increasing light illumination from 10^{-04} up to 1 sun equivalent. Nyquist representation (a & c), with two characteristic semi-circles observed. Capacitance (absolute magnitude) vs frequency Bode plots (b & d), with HF plateau and additional LF transition from capacitive polarization towards inductive loops. DD simulated raw data (circles) with fit functions (solid lines) to the selected ECM (as inset shown in main **Fig. 2 (d)**). In addition to the parameters in Table S4.1: μ_{PK} = 20

$cm^2V^{-1}s^{-1}$, $\tau_{PK}^{SRH} = 10$ ns and $N_{ion} = 10^{+18} cm^{-3}$. (a-b) V_{bi}=0.6 V vs (c-d) V_{bi}=0.8 V.

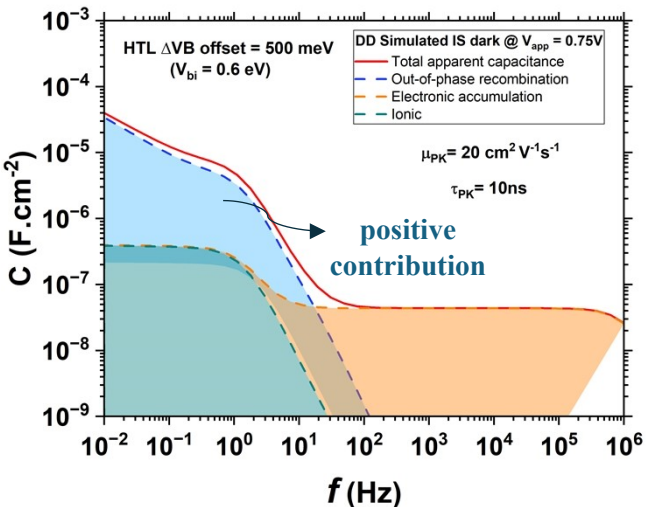

(a)

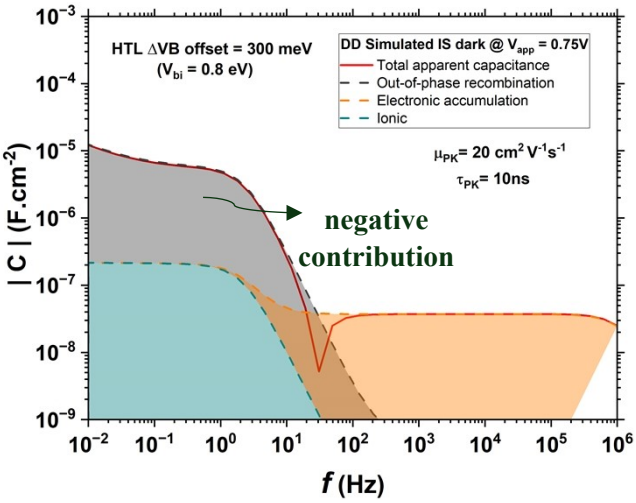

(b)

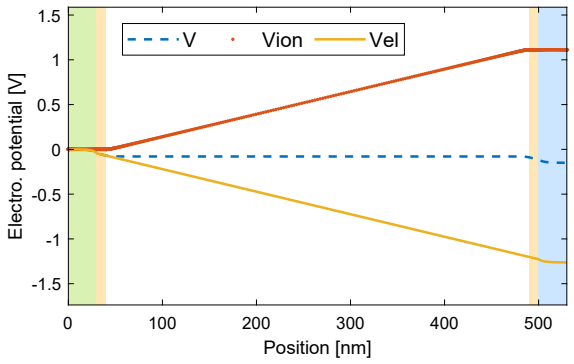

(c)

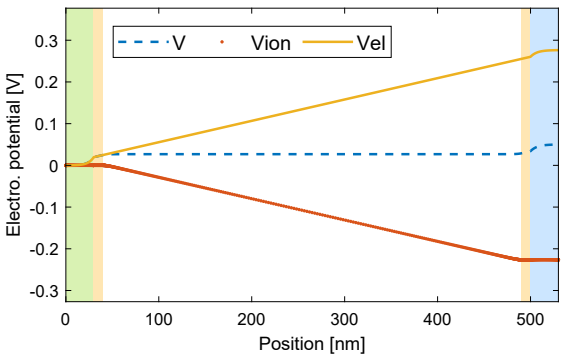

(d)

(f)

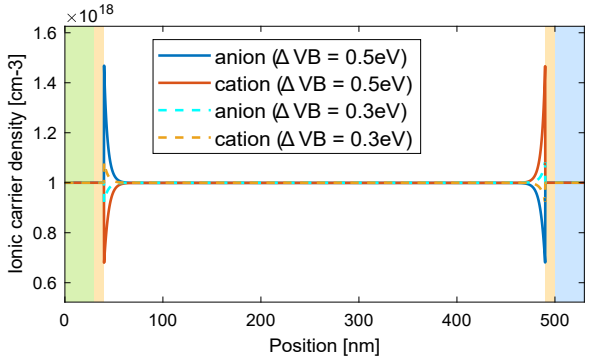

(e)

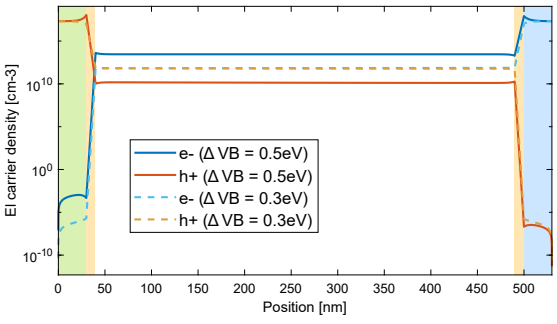

Figure S4.11 Effect of varying ΔVB band offset for majority carriers at PK/HTL interface, defining V_{bi} and modulating charge recombination. DD simulated Capacitance vs frequency at 0.75V bias in dark for: (a) $^{V_{bi}}$=0.6 V vs (b) $^{V_{bi}}$=0.8 V. Input parameters additionally to Table S4.1: μ_{PK} = 20 cm^{2}V^{-1}s^{-1}, τ_{PK}^{SRH} = 10 ns and N_{ion}= 10^{+18}cm^{-3}. Total capacitance (red) decomposition into HF dominated electronic accumulation (green), ionic accumulation and LF phase-delayed recombination yielding in either: a positive effective capacitance in (a); or effective "negative" capacitance in (b) where the total response is equivalent to the appearance of inductive effects in IS measurements at LF. For which, the corresponding potential distributions are presented in (c) and (d), respectively. The total V (dashed blue) results from the balancing of electronic (yellow solid) and ionic (orange solid) electrostatics. Likewise, the corresponding N_{ion} (solid lines) and free carriers' concentration profiles (dashed lines) are presented in (e) and (f), respectively.

IS fits to selected ECM: R_{LF} and C_{LF} vs J_{SC} at different light illumination intensities

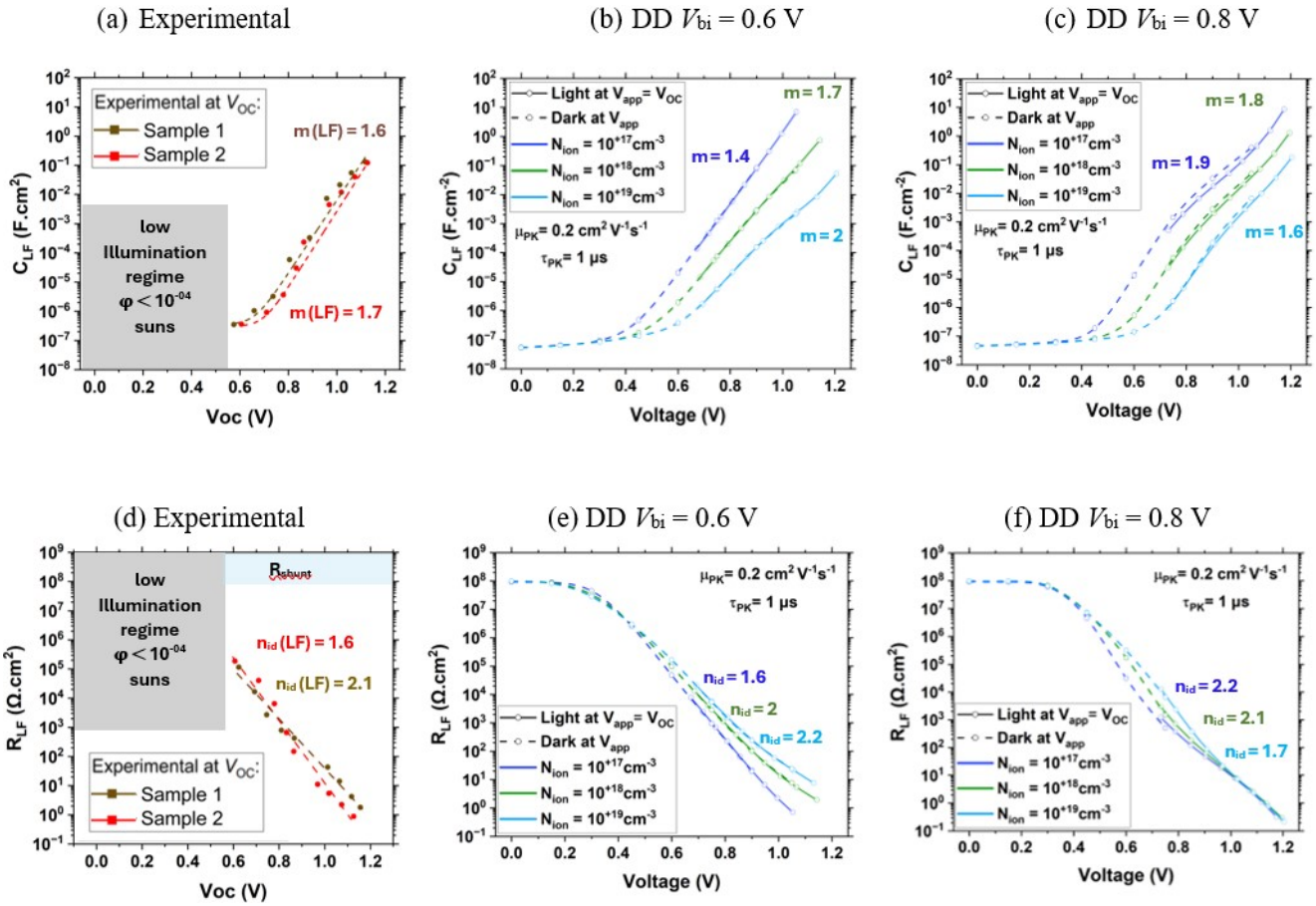

Figure S4.12 C_{LF} (a-c) and R_{LF} (d-f) evolution at open-circuit (V_{oc}) increasing light illumination from 10^{-04} to 1 sun equivalent, obtained by IS fits to selected ECM (as depicted in inset of main **Fig. 2 (d)**). Comparison of experimental (a & d) versus DD simulated IS (b-c & e-f) measurements varying N_{ion} at $^{V_{bi}}$=0.6 V (b & e) vs $^{V_{bi}}$=0.8 V (c & f). Experimental IS for two representative samples of selected PSC architecture. The $^{n_{id}}$ values estimated from R_{LF} were derived using a 1-diode model.

For the R_{LF}–V_{OC} in **Fig S4.12 (d-f)**, similarly as observed at SC conditions in **Fig. S4.6**, we notice that the interfacial band offsets (e.g., studied here by varying ΔVB) play a role in ionic-modulated dynamics, by tuning the -Im(Z) component at low frequencies through phase-delayed recombination (^{A_R}). For the

C_{LF} in **Fig S4.12 (a-c)**, ion-modulated delayed recombination can also contribute to the -Im(Z) component at low frequencies. The latter can in some additional cases also introduce a transition from positive (effective capacitance) to negative (chemical inductance) contributions of ^{A_R} to -Im(Z), for instance when reducing $^{N_{ion}}$ from 10^{17} to 10^{15} cm^{-3} or $^{\tau_{PK}^{SRH}}$ from 1μs to 10 ns. Nevertheless, under OC conditions the low frequency contributions for R and C are not purely ion-related, as an additional $C_{diff}(V)$ is involved in the charge injection under forward voltage bias, which yields in a non-constant τ_{LF} as shown in **Fig. S4.14**.

IS fits to selected ECM: R_{HF} and R_{LF} vs V_{OC} under low R_{SH} at different N_{ion}

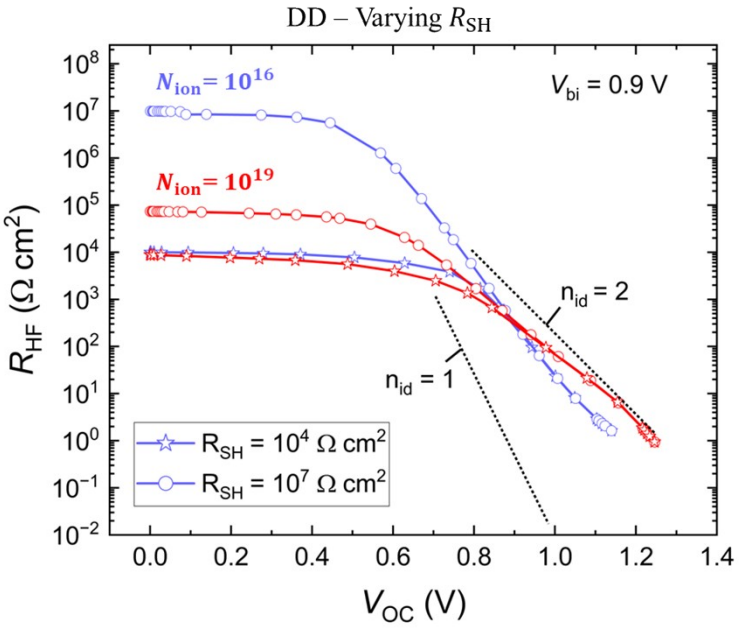

Figure S4.13 Simulated IS fits to ECM (as depicted in inset of main **Fig. 2 (d)**), with R_{HF} as a function of V_{OC} under increasing light illumination from 10^{-04} to 1 sun. Effect of varying $^{N_{ion}} = [10^{16}, 10^{19}]$ cm^{-3} and R_{SH} $= [10^6, 10^7, 10^8]\ \Omega\ cm^2$; with fixed $^{V_{bi}}$=0.6, μ_{PK}=20 $cm^2V^{-1}s^{-1}$ and τ_{PK}^{SRH} =1 μs. Dashed lines limits corresponding to $^{n_{id}}$ values between 1 and 2.

IS fits to selected ECM: τ_{HF} and τ_{LF} vs J_{SC} at different light illumination intensities

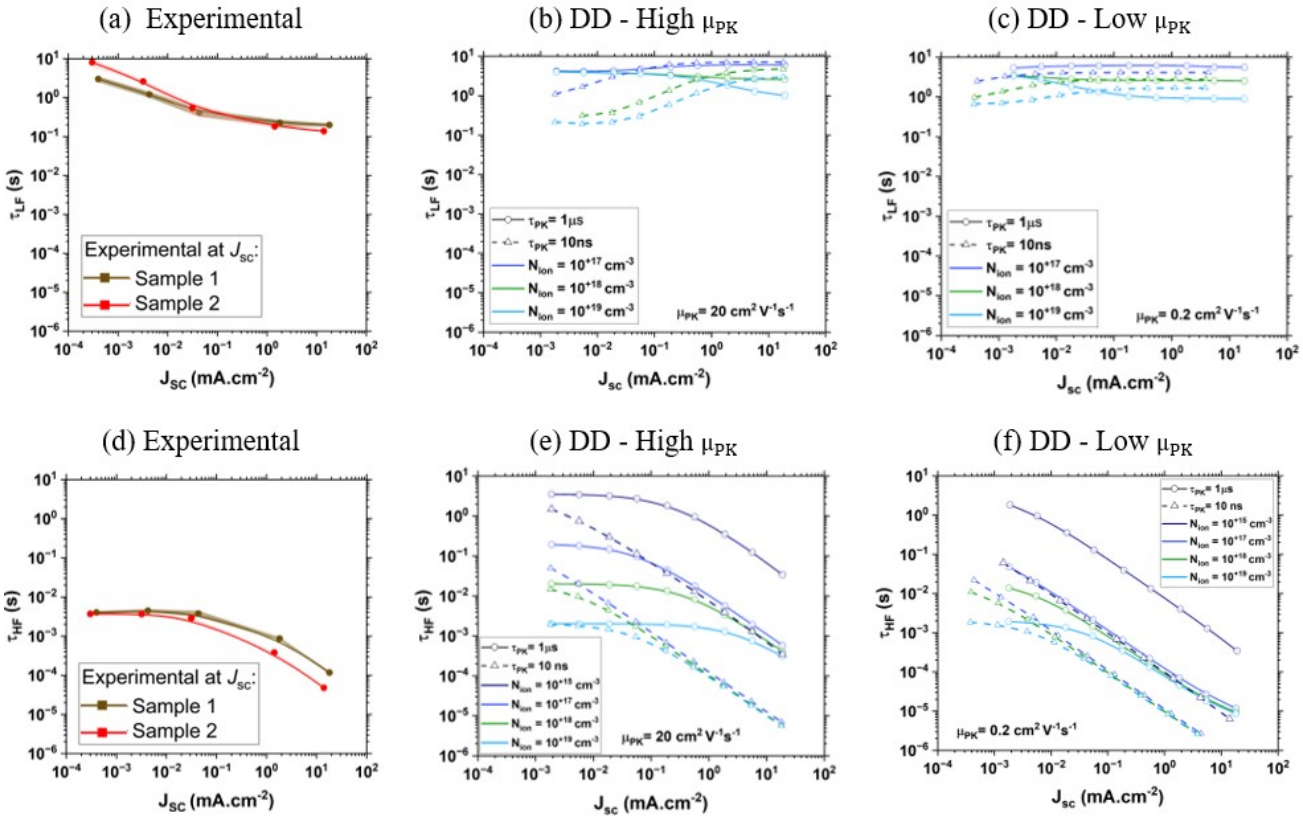

Figure S4.13 PSC characteristic times τ_{HF} (a-c) and τ_{LF} (d-f) vs J_{sc} under different light illuminations from 10^{-04} up to 1 sun, obtained from fits of IS to ECM (as inset in main **Fig. 2 (d)**). Experimental (a & d) vs DD simulated (b-c & e-f) results varying $N_{ion} = [10^{15} - 10^{19}]$ cm^{-3}, $\mu_{PK}\ (cm^2V^{-1}s^{-1}) = \{0.2, 20\}$ and $\tau_{PK}^{SRH}(s) = \{10^{-06},\ 10^{-08}\}$. DD simulations at high (b & e) and low μ_{PK} (c & f) with fixed V_{bi}=0.6 V. Experimental IS measurements (a & c) for two representative samples of selected PSC with Au-opaque top contact electrode.

IS fits to selected ECM: τ_{HF} and τ_{LF} vs V_{OC} at different light illumination intensities

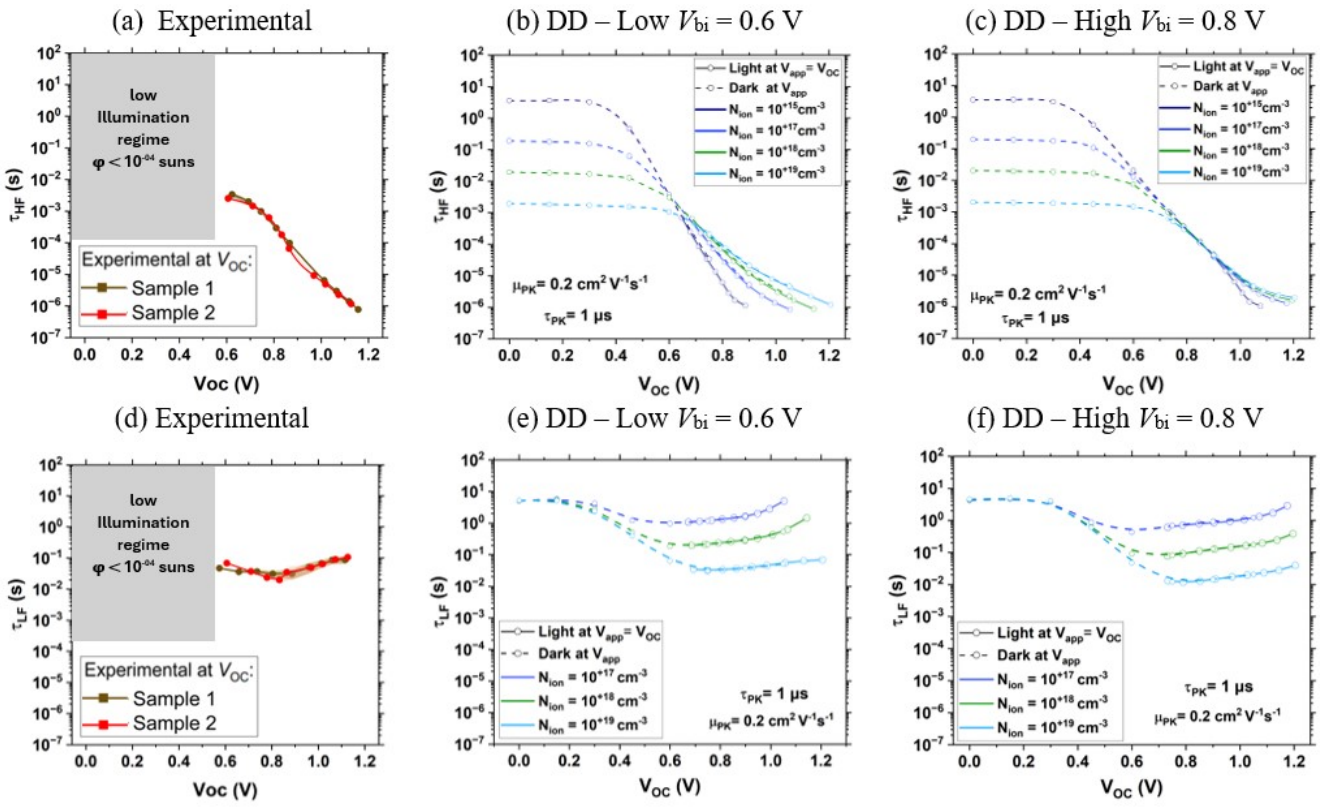

Figure S4.14 PSC characteristic times τ_{HF} (a-c) and τ_{LF} (d-f) vs V_{OC} under different light illuminations from 10^{-04} up to 1 sun, obtained from fits of IS to ECM (as inset in main **Fig. 2 (d)**). Experimental (a & d) vs DD simulated (b-c & e-f) results varying $N_{ion} = [10^{15} - 10^{19}]$ cm^{-3}, $V_{bi}\,(V) = \{0.6, 0.8\}$ and $\tau_{PK}^{SRH}(s) = \{10^{-06},\ 10^{-08}\}$. DD simulations at high (b & e) and low V_{bi} (c & f) at fixed $\mu_{PK} = 0.2\ cm^2V^{-1}s^{-1}$. Experimental IS measurements (a & c) for two representative samples of selected PSC with Au-opaque top contact electrode.

Experimental IS fits to selected ECM

Table S4.1: IS fits summary obtained from experimental measurements in PSC sample 1, in dark and under increasing light illumination from 10^{-04} up to 1 sun equivalent, at 0V(short-circuit) and at $V_{OC} = V_{app}$.

Sample 1 at 0V											
φ (Suns)	R_S (Ω*cm²)	R_{HF} (Ω*cm²)	R_{LF} (Ω*cm²)	R_{Total} (Ω*cm²)	$Q_{0\ HF}$ (nF.cm^{-2}.s$^{\alpha-1}$)	α_{HF}	C_{HF} (F.cm^{-2})	$Q_{0\ LF}$ (nF.cm^{-2}.s$^{\alpha-1}$)	α_{LF}	C_{LF} (F.cm^{-2})	Total error

0	1.28	4.92E+04	6.54E+07	6.54E+07	1.45E+01	0.98	6.3E-08	3.60E+01	0.94	2.04E-07	1.65%
1E-4	1.22	5.54E+04	1.51E+07	1.52E+07	1.77E+01	0.97	7.24E-08	3.78E+01	0.94	1.98E-07	2.66%
1E-3	1.18	5.60E+04	6.48E+06	6.53E+06	2.03E+01	0.96	7.93E-08	3.76E+01	0.94	1.85E-07	2.56%
1E-2	1.15	4.49E+04	1.76E+06	1.81E+06	2.21E+01	0.95	8.34E-08	5.21E+01	0.91	2.34E-07	3.09%
0.1	1.06	8.08E+03	8.30E+04	9.11E+04	3.75E+01	0.92	1.06E-07	7.51E+02	0.78	2.69E-06	6.15%
1	1.32	8.20E+02	6.62E+03	7.44E+03	8.31E+01	0.88	1.42E-07	9.30E+03	0.72	2.98E-05	4.12%
Sample 1 at *V*oc											
φ (Suns)	**R_S (Ω*cm^2)**	**R_{HF} (Ω*cm^2)**	**R_{LF} (Ω*cm^2)**	**R_{Total} (Ω*cm^2)**	**$Q_{0\ HF}$ (nF.cm^{-2}.s$^{\alpha-1}$)**	**α_{HF}**	**C_{HF} (F.cm^{-2})**	**$Q_{0\ LF}$ (nF.cm^{-2}.s$^{\alpha-1}$)**	**α_{LF}**	**C_{LF} (F.cm^{-2})**	**Total error**
1E-4	1.15	4.18E+04	1.17E+05	1.58E+05	2.12E+01	0.96	8.00E-08	8.46E+01	0.86	2.61E-07	2.93%
3E-4	1.13	2.42E+04	1.67E+04	4.09E+04	2.31E+01	0.95	8.26E-08	4.60E+02	0.73	9.15E-07	2.82%
1E-3	1.09	1.17E+04	2.71E+03	1.44E+04	2.54E+01	0.94	8.41E-08	3.45E+03	0.73	9.86E-06	2.72%
3E-3	1.08	3.59E+03	7.97E+02	4.39E+03	2.75E+01	0.94	8.17E-08	7.87E+03	0.89	3.08E-05	2.41%
1E-2	1.09	1.23E+03	4.28E+02	1.66E+03	2.88E+01	0.94	7.85E-08	1.13E+04	0.95	4.84E-05	2.10%
3E-2	1.16	8.24E+01	4.33E+01	1.27E+02	4.10E+01	0.92	7.79E-08	2.14E+08	0.87	2.18E+00	1.32%
0.1	1.22	3.10E+01	1.43E+01	4.64E+01	6.23E+01	0.91	9.58E-08	1.04E+06	0.83	3.80E-03	1.59%
0.3	1.39	1.13E+01	4.24E+00	1.69E+01	5.89E+01	0.94	1.24E-07	5.27E+06	0.80	2.09E-02	2.72%
1	1.50	5.21E+00	1.81E+00	8.52E+00	5.47E+01	0.96	1.49E-07	1.35E+07	0.79	5.65E-02	1.28%

Table S4.2: IS fits summary obtained from experimental measurements in PSC sample 2, in dark and under increasing light illumination from 10^{-04} up to 1 sun equivalent, at 0V(short-circuit) and at $V_{OC} = V_{app}$.

Sample 2 at 0V											
φ (Suns)	**R_S (Ω*cm^2)**	**R_{HF} (Ω*cm^2)**	**R_{LF} (Ω*cm^2)**	**R_{Total} (Ω*cm^2)**	**$Q_{0\ HF}$ (nF.cm^{-2}.s$^{\alpha-1}$)**	**α_{HF}**	**C_{HF} (F.cm^{-2})**	**$Q_{0\ LF}$ (nF.cm^{-2}.s$^{\alpha-1}$)**	**α_{LF}**	**C_{LF} (F.cm^{-2})**	**Total error**
0	3.69	5.01E+04	9.33E+07	9.34E+07	3.55E+01	0.98	6.34E-08	9.18E+01	0.93	2.31E-07	2.30%
1E-4	3.24	4.88E+04	3.15E+07	3.15E+07	3.86E+01	0.97	7.54E-08	9.63E+01	0.92	2.57E-07	1.64%
1E-3	3.20	4.80E+04	1.08E+07	1.09E+07	3.87E+01	0.97	7.56E-08	9.77E+01	0.93	2.38E-07	1.57%
1E-2	3.20	3.80E+04	1.86E+06	1.89E+06	3.89E+01	0.97	7.55E-08	1.35E+02	0.90	2.89E-07	3.85%
0.1	3.11	4.66E+03	4.15E+04	4.62E+04	4.96E+01	0.96	8.1E-08	2.69E+03	0.79	4.35E-06	3.72%
1	3.15	4.71E+02	3.28E+03	3.75E+03	1.01E+02	0.92	1.02E-07	2.77E+04	0.78	4.19E-05	3.37%
Sample 2 at *V*oc											
φ (Suns)	**R_S (Ω*cm^2)**	**R_{HF} (Ω*cm^2)**	**R_{LF} (Ω*cm^2)**	**R_{Total} (Ω*cm^2)**	**$Q_{0\ HF}$ (nF.cm^{-2}.s$^{\alpha-1}$)**	**α_{HF}**	**C_{HF} (F.cm^{-2})**	**$Q_{0\ LF}$ (nF.cm^{-2}.s$^{\alpha-1}$)**	**α_{LF}**	**C_{LF} (F.cm^{-2})**	**Total error**
1E-4	3.26	3.28E+04	1.88E+05	2.21E+05	4.00E+01	0.97	7.69E-08	2.36E+02	0.85	3.63E-07	2.49%
3E-4	3.20	1.87E+04	4.06E+04	5.93E+04	4.14E+01	0.97	7.73E-08	6.76E+02	0.82	9.11E-07	1.95%
1E-3	3.22	8.14E+03	6.47E+03	1.46E+04	4.20E+01	0.97	7.59E-08	2.67E+03	0.83	3.66E-06	1.90%
3E-3	3.24	2.36E+03	6.60E+02	3.03E+03	4.37E+01	0.97	7.60E-08	1.88E+04	0.85	3.01E-05	1.74%
1E-2	3.34	8.32E+02	1.50E+02	9.85E+02	4.78E+01	0.97	7.91E-08	1.60E+05	0.70	2.34E-04	1.84%
3E-2	3.52	6.29E+01	1.11E+01	7.75E+01	1.46E+02	0.93	1.46E-07	2.32E+06	0.84	4.47E-03	2.23%
0.1	3.50	2.60E+01	5.41E+00	3.49E+01	2.20E+02	0.92	1.88E-07	6.04E+06	0.84	1.19E-02	1.96%
0.3	3.43	9.37E+00	2.23E+00	1.50E+01	2.96E+02	0.92	2.44E-07	1.95E+07	0.81	4.02E-02	1.52%
1	3.40	3.78E+00	8.80E-01	8.07E+00	3.12E+02	0.94	3.08E-07	5.37E+07	0.77	1.21E-01	1.53%

DD simulated IS fits to selected ECM

Table S4.3: IS fits summary obtained from DD simulations, for a PSC with low μ_{PK}, in dark and under increasing light illumination from 10^{-04} up to 1 sun equivalent, at 0V(short-circuit) and at $V_{OC} = V_{app}$.

DD – Low μ_{PK} at 0V ($N_{ion} = 10^{18}$ cm^{-3})											
φ (Suns)	R_S (Ω*cm^2)	R_{HF} (Ω*cm^2)	R_{LF} (Ω*cm^2)	R_{Total} (Ω*cm^2)	$Q_{0\ HF}$ (nF.cm^{-2}.s$^{\alpha-1}$)	α_{HF}	C_{HF} (F.cm^{-2})	$Q_{0\ LF}$ (nF.cm^{-2}.s$^{\alpha-1}$)	α_{LF}	C_{LF} (F.cm^{-2})	Total error
0	1.95	6.59E+05	9.80E+07	9.87E+07	2.94E+01	1.00	2.94E-08	5.21E+01	1.00	5.23E-08	0.04%
1E-4	1.95	4.58E+05	4.46E+07	4.50E+07	2.93E+01	1.00	2.93E-08	7.62E+01	0.99	7.72E-08	0.38%
3E-4	1.96	2.86E+05	2.46E+07	2.49E+07	2.92E+01	1.00	2.92E-08	1.23E+02	0.98	1.25E-07	0.64%
1E-3	1.96	1.25E+05	9.56E+06	9.69E+06	2.92E+01	1.00	2.92E-08	2.87E+02	0.98	2.92E-07	0.87%
3E-3	1.97	4.79E+04	3.48E+06	3.53E+06	2.92E+01	1.00	2.94E-08	7.54E+02	0.98	7.68E-07	0.99%
1E-2	1.99	1.52E+04	1.08E+06	1.09E+06	2.94E+01	1.00	2.94E-08	2.39E+03	0.98	2.43E-06	1.07%
3E-2	2.05	5.18E+03	3.62E+05	3.67E+05	3.01E+01	1.00	3.01E-08	7.06E+03	0.98	7.18E-06	1.13%
0.1	2.23	1.58E+03	1.08E+05	1.10E+05	3.26E+01	1.00	3.19E-08	2.35E+04	0.98	2.39E-05	1.23%
0.3	2.62	5.42E+02	3.55E+04	3.61E+04	3.96E+01	0.99	3.69E-08	7.12E+04	0.98	7.23E-05	1.43%
1	3.22	1.75E+02	1.01E+04	1.03E+04	5.84E+01	0.99	5.23E-08	2.47E+05	0.99	2.51E-04	1.74%
DD – High μ_{PK} at Voc ($N_{ion} = 10^{18}$ cm^{-3})											
φ (Suns)	R_S (Ω*cm^2)	R_{HF} (Ω*cm^2)	R_{LF} (Ω*cm^2)	R_{Total} (Ω*cm^2)	$Q_{0\ HF}$ (nF.cm^{-2}.s$^{\alpha-1}$)	α_{HF}	C_{HF} (F.cm^{-2})	$Q_{0\ LF}$ (nF.cm^{-2}.s$^{\alpha-1}$)	α_{LF}	C_{LF} (F.cm^{-2})	Total error
1E-4	3.03	1.56E+04	1.33E+04	2.89E+04	4.13E+01	1.00	4.12E-08	1.52E+04	0.97	1.48E-05	0.40%
3E-4	3.10	5.30E+03	4.07E+03	9.37E+03	4.35E+01	1.00	4.31E-08	5.42E+04	0.96	5.28E-05	0.51%
1E-3	3.24	1.60E+03	1.16E+03	2.76E+03	4.84E+01	1.00	4.71E-08	2.10E+05	0.96	2.05E-04	0.77%
3E-3	3.46	5.38E+02	3.77E+02	9.19E+02	5.83E+01	0.99	5.53E-08	7.04E+05	0.95	6.89E-04	1.14%
1E-2	3.66	1.64E+02	1.14E+02	2.81E+02	7.95E+01	0.99	7.49E-08	2.60E+06	0.94	2.55E-03	1.32%
3E-2	3.59	5.60E+01	3.97E+01	9.93E+01	1.15E+02	1.00	1.10E-07	8.53E+06	0.91	8.40E-03	1.11%
0.1	3.36	1.77E+01	1.35E+01	3.45E+01	1.78E+02	1.00	1.74E-07	3.12E+07	0.85	3.16E-02	1.06%
0.3	3.20	6.31E+00	5.42E+00	1.49E+01	2.64E+02	1.00	2.62E-07	1.04E+08	0.77	1.19E-01	1.39%
1	3.11	2.11E+00	1.94E+00	7.16E+00	4.32E+02	1.00	4.17E-07	4.28E+08	0.67	7.47E-01	1.88%

Table S4.4: IS fits summary obtained from DD simulations, for a PSC with high μ_{PK}, in dark and under increasing light illumination from 10^{-04} up to 1 sun equivalent, at 0V(short-circuit) and at $V_{OC} = V_{app}$.

DD – High μ_{PK} at 0V ($N_{ion} = 10^{18}$ cm^{-3})											
φ (Suns)	R_S (Ω*cm^2)	R_{HF} (Ω*cm^2)	R_{LF} (Ω*cm^2)	R_{Total} (Ω*cm^2)	$Q_{0\ HF}$ (nF.cm^{-2}.s$^{\alpha-1}$)	α_{HF}	C_{HF} (F.cm^{-2})	$Q_{0\ LF}$ (nF.cm^{-2}.s$^{\alpha-1}$)	α_{LF}	C_{LF} (F.cm^{-2})	Total error
0	1.95	6.59E+05	9.80E+07	9.87E+07	2.94E+01	1.00	2.94E-08	5.21E+01	1.00	5.23E-08	0.04%
1E-4	1.95	6.55E+05	7.78E+07	7.84E+07	2.94E+01	1.00	2.94E-08	5.25E+01	1.00	5.28E-08	0.04%

3E-4	1.95	6.48E+05	7.37E+07	7.44E+07	2.94E+01	1.00	2.94E-08	5.31E+01	1.00	5.33E-08	0.05%
1E-3	1.95	6.27E+05	6.91E+07	6.97E+07	2.94E+01	1.00	2.94E-08	5.50E+01	1.00	5.53E-08	0.09%
3E-3	1.95	5.73E+05	6.05E+07	6.11E+07	2.94E+01	1.00	2.93E-08	6.03E+01	0.99	6.08E-08	0.18%
1E-2	1.95	4.42E+05	4.24E+07	4.28E+07	2.93E+01	1.00	2.93E-08	7.89E+01	0.99	8.00E-08	0.40%
3E-2	1.96	2.69E+05	2.28E+07	2.31E+07	2.92E+01	1.00	2.92E-08	1.31E+02	0.98	1.34E-07	0.66%
0.1	1.98	1.14E+05	8.69E+06	8.80E+06	2.92E+01	1.00	2.94E-08	3.15E+02	0.98	3.21E-07	0.87%
0.3	2.01	4.30E+04	3.09E+06	3.14E+06	2.94E+01	1.00	2.95E-08	8.47E+02	0.98	8.62E-07	0.97%
1	2.12	1.33E+04	9.03E+05	9.17E+05	2.99E+01	1.00	3.01E-08	2.81E+03	0.98	2.85E-06	1.02%
DD – High μ_{PK} at *Voc* (N_{ion} = 10^{18} cm^{-3})											
φ (Suns)	**R_S (Ω*cm²)**	**R_{HF} (Ω*cm²)**	**R_{LF} (Ω*cm²)**	**R_{Total} (Ω*cm²)**	**$Q_{0\ HF}$ (nF.cm^{-2}.s$^{α-1}$)**	**α_{HF}**	**C_{HF} (F.cm^{-2})**	**$Q_{0\ LF}$ (nF.cm^{-2}.s$^{α-1}$)**	**α_{LF}**	**C_{LF} (F.cm^{-2})**	**Total error**
1E-4	2.99	1.43E+04	1.11E+04	2.54E+04	4.14E+01	1.00	4.13E-08	1.79E+04	0.96	1.74E-05	0.39%
3E-4	3.00	4.84E+03	3.37E+03	8.21E+03	4.34E+01	1.00	4.33E-08	6.44E+04	0.96	6.26E-05	0.44%
1E-3	3.01	1.46E+03	9.56E+02	2.42E+03	4.78E+01	1.00	4.77E-08	2.51E+05	0.95	2.45E-04	0.50%
3E-3	3.02	4.89E+02	3.11E+02	8.03E+02	5.70E+01	1.00	5.68E-08	8.49E+05	0.94	8.29E-04	0.56%
1E-2	3.02	1.49E+02	9.37E+01	2.46E+02	7.89E+01	1.00	7.84E-08	3.17E+06	0.92	3.11E-03	0.65%
3E-2	3.02	5.10E+01	3.29E+01	8.69E+01	1.17E+02	1.00	1.16E-07	1.05E+07	0.89	1.03E-02	0.75%
0.1	3.02	1.61E+01	1.14E+01	3.05E+01	1.82E+02	1.00	1.82E-07	3.83E+07	0.81	3.97E-02	0.95%
0.3	3.02	5.73E+00	4.60E+00	1.33E+01	2.68E+02	1.00	2.71E-07	1.28E+08	0.72	1.58E-01	1.30%
1	3.01	1.91E+00	1.59E+00	6.51E+00	4.29E+02	1.00	4.29E-07	5.47E+08	0.62	1.21E+00	1.74%

Impact of electron-hole mobility (μ_{PK}) imbalances on IS fits at SC

We note that the μ_{PK} values extracted in this work correspond to the effective electronic mobility in the perovskite layer, for long-range charge transport, once incorporated into the full PSC stack. Carrier mobilities, of up to ~100 $cm^2V^{-1}s^{-1}$, have been reported in perovskite single crystals [49]. Yet, it is well established that the electron and hole mobilities in perovskite films are significantly reduced, compared to single crystals, due to presences of defects and grain boundaries. Indeed, recent studies report long-range μ_{PK} values, for perovskites with similar triple cation (FAMACs) compositions, between the range of 0.2 - 2 $cm^2V^{-1}s^{-1}$; and with minor imbalances, typically μ_h/μ_e ratios of up to 3:1 [50,51]. However, stronger imbalances can be expected, with μ_h ~10x times higher than μ_e, for films of superior quality [52].

In all the main DD simulations of this study, we equally varied μ_{PK} in the PK layer for the sake of analysis simplicity, although real PSC devices may exhibit a non-negligible asymmetry between the electron–hole mobility. Thus, we provide complementary IS fits in **Fig S4.15**, for low **(a-b)** and high **(c-d)** μe/μh imbalances in the perovskite layer. In all cases, we did not observe any difference for the limiting effect of N_{ion} on the R'_{SH-HF} and R'_{SH-LF} plateaus at low light illumination (Ψ) conditions. However, in the case of high μ_h/μ_e imbalances, a variation in the *R*-

J_{SC} profiles (dashed) is expected in the region dominated by R_{rec} towards high Ψ, compared to the reference cases with equally varied μ_{PK}=μ_h=μ_e (solid); defined by a constant offset at HF, and the additional modulation of R_{rec} at LF with N_{ion} accumulation at PK/CTLs interfaces. At LF, the effect of reducing one carrier mobility relative to the other is not symmetric, due to the asymmetric energy band offsets defined in the DD model for the case of a low V_{bi} = 0.6V.

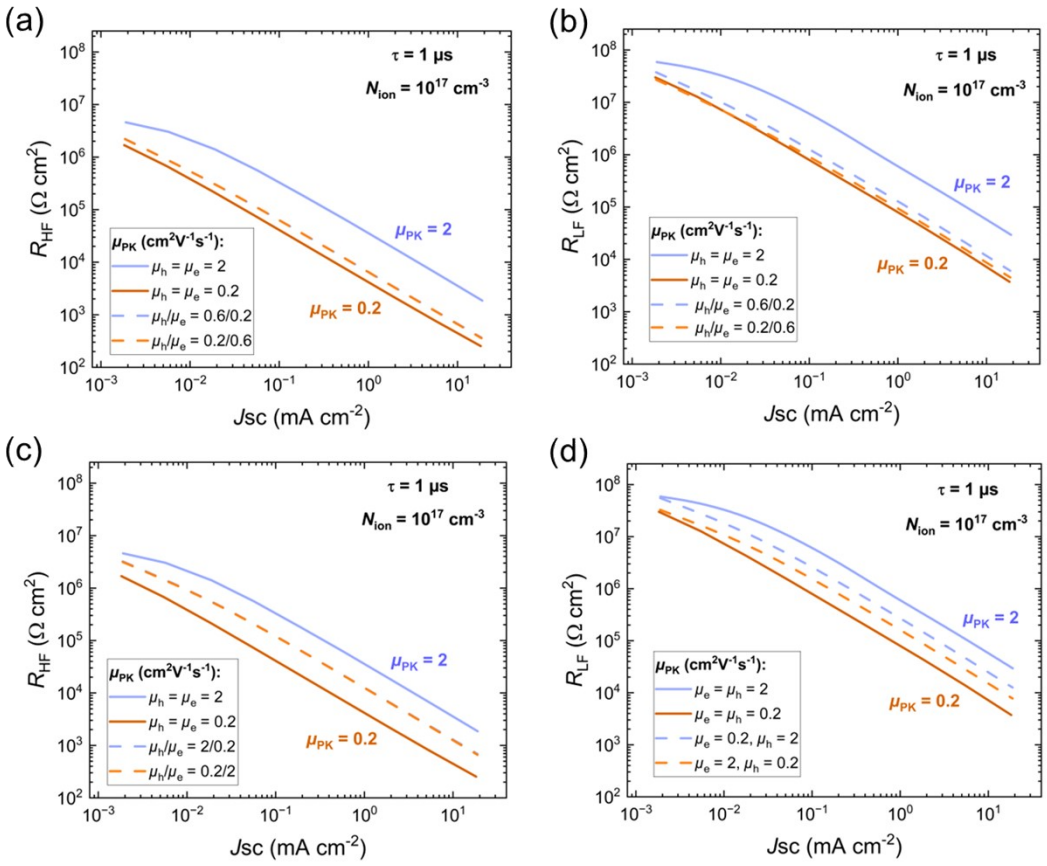

Figure S4.15 Simulated IS fits to selected ECM (as inset in **Fig. 2 (d)**), with R_{HF} (a & c) and R_{LF} (b & d) as a function of J_{SC} under different light illuminations from 10^{-04} to 1 sun equivalent. Fixed ion concentration set at $N_{ion} = 10^{17}$ cm^{-3} with $R_{SH} = 10^8\ \Omega\ cm^2$, V_{bi}=0.6V and τ_{PK}^{SRH}=1 μs. Fixed asymmetry of 3:1 and 10:1 in the electronic $\mu_{h/}\mu_e$ mobility (dashed) versus equally varied μ_{PK}=μ_e=$\mu_h = [0.2, 2]\ cm^2V^{-1}s^{-1}$ of the PK layer.

IS fits to selected ECM: extended DD simulations at J_{SC} down to 0.1 mHz

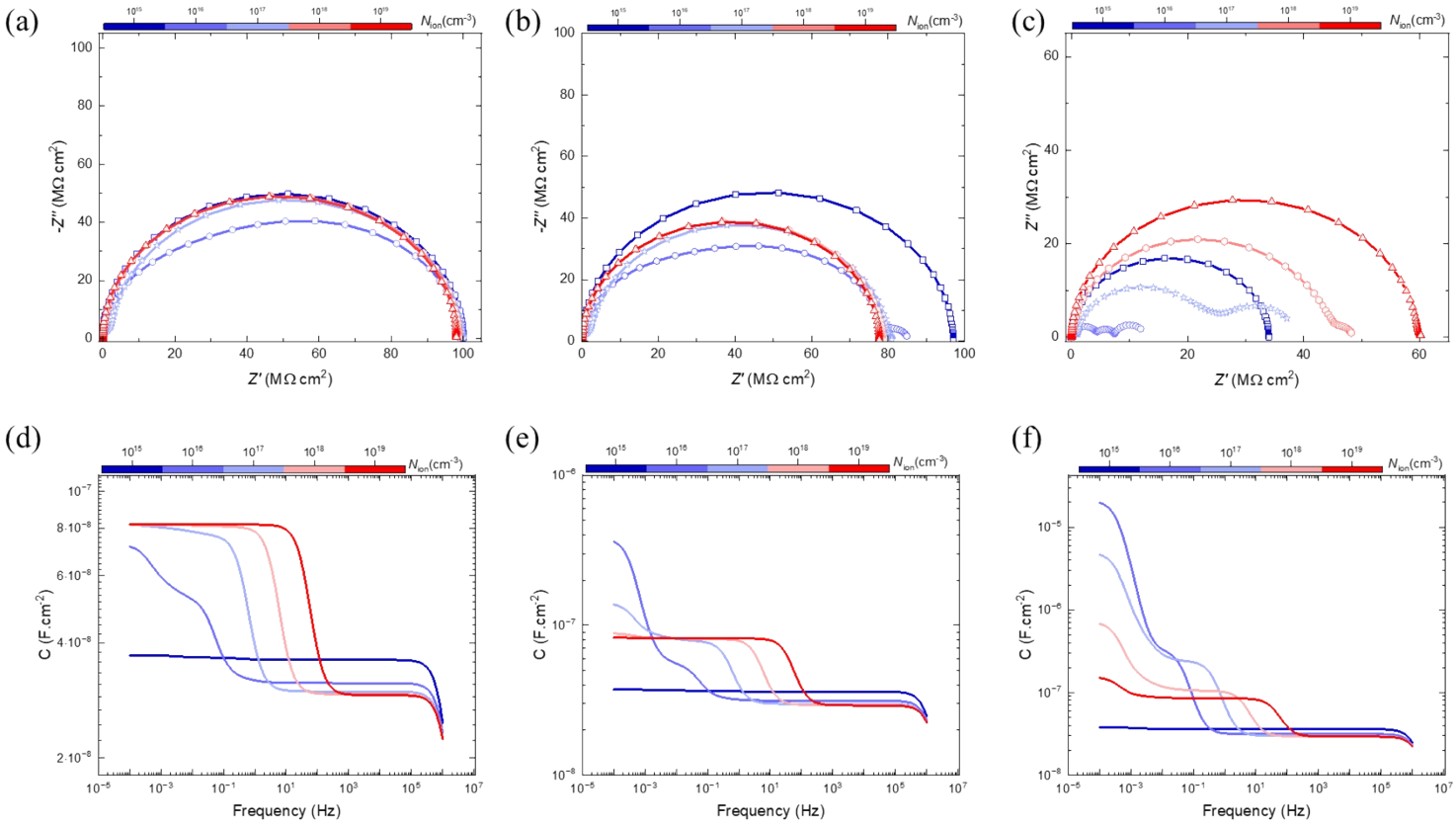

Figure S4.16 DD simulated IS in dark 0V and at J_{sc} with low light illumination intensities, Ψ = {0, 10^{-04}, 10^{-02}} suns equivalent with varying $N_{ion} = [10^{15} - 10^{19}]$ cm^{-3}. Results in Nyquist representation (a-c), with two characteristic semi-circles observed down to 0.1mHz. Corresponding capacitance vs frequency Bode plots (d-f), with HF plateau and additional polarization towards LF. DD simulated raw data (circles) data, plotted along with equivalent fit functions (solid lines) to selected ECM (as inset shown in **Fig. 2 (d)**). In addition to the DD parameters indicated in Table S1: V_{bi}=0.6 V, $\mu_{PK} = 20\ cm^2V^{-1}s^{-1}$, τ_{PK}^{SRH} = 1µs and R_{SH} = $10^8\ \Omega cm^2$.

Additional references

[1] P. Calado, I. Gelmetti, B. Hilton, M. Azzouzi, J. Nelson, and P.R.F. Barnes, "Driftfusion: an open source code for simulating ordered semiconductor devices with mixed ionic-electronic conducting materials in one dimension," J. Comput. Electron. **21**(4), 960–991 (2022).

[2] C. Eames, J.M. Frost, P.R.F. Barnes, B.C. O'Regan, A. Walsh, and M.S. Islam, "Ionic transport in hybrid lead iodide perovskite solar cells," Nat. Commun. **6**(1), 7497 (2015).

[3] X. Qiu, Y. Liu, W. Li, and Y. Hu, "Traps in metal halide perovskites: characterization and passivation," Nanoscale **12**(44), 22425–22451 (2020).

[4] P. Caprioglio, C.M. Wolff, O.J. Sandberg, A. Armin, B. Rech, S. Albrecht, D. Neher, and M. Stolterfoht, "On the Origin of the Ideality Factor in Perovskite Solar Cells," Adv. Energy Mater. **10**(27), 2000502 (2020).

[5] O. Almora, P. López-Varo, R. Escalante, J. Mohanraj, L.F. Marsal, S. Olthof, and J.A. Anta, "Instability analysis of perovskite solar cells via short-circuit impedance spectroscopy: A case study on NiOx passivation," J. Appl. Phys. **136**(9), 094502 (2024).

[6] J. Thiesbrummel, S. Shah, E. Gutierrez-Partida, F. Zu, F. Peña-Camargo, S. Zeiske, J. Diekmann, F. Ye, K.P. Peters, K.O. Brinkmann, P. Caprioglio, A. Dasgupta, S. Seo, F.A. Adeleye, J. Warby, Q. Jeangros, F. Lang, S. Zhang, S. Albrecht, T. Riedl, A. Armin, D. Neher, N. Koch, Y. Wu, V.M. Le Corre, H. Snaith, and M. Stolterfoht, "Ion-induced field screening as a dominant factor in perovskite solar cell operational stability," Nat. Energy **9**(6), 664–676 (2024).

[7] W. Clarke, G. Richardson, and P. Cameron, "Understanding the Full Zoo of Perovskite Solar Cell Impedance Spectra with the Standard Drift-Diffusion Model," Adv. Energy Mater. **14**(32), 2400955 (2024).

[8] A. Guerrero, J. Bisquert, and G. Garcia-Belmonte, "Impedance Spectroscopy of Metal Halide Perovskite Solar Cells from the Perspective of Equivalent Circuits," Chem. Rev. **121**(23), 14430–14484 (2021).

[9] E. Ghahremanirad, O. Almora, S. Suresh, A.A. Drew, T.H. Chowdhury, and A.R. Uhl, "Beyond Protocols: Understanding the Electrical Behavior of Perovskite Solar Cells by Impedance Spectroscopy," Adv. Energy Mater. **13**(30), 2204370 (2023).

[10] E. Von Hauff, and D. Klotz, "Impedance spectroscopy for perovskite solar cells: characterisation, analysis, and diagnosis," J. Mater. Chem. C **10**(2), 742–761 (2022).

[11] D.A. Jacobs, H. Shen, F. Pfeffer, J. Peng, T.P. White, F.J. Beck, and K.R. Catchpole, "The Two Faces of Capacitance: New Interpretations for Electrical Impedance Measurements of Perovskite Solar Cells and Their Relation to Hysteresis," J. Appl. Phys. **124**(22), 225702 (2018).

[12] C. Gonzales, A. Guerrero, and J. Bisquert, "Spectral properties of the dynamic state transition in metal halide perovskite-based memristor exhibiting negative capacitance," Appl. Phys. Lett. **118**(7), 073501 (2021).

[13] S. Ravishankar, Z. Liu, U. Rau, and T. Kirchartz, "Multilayer Capacitances: How Selective Contacts Affect Capacitance Measurements of Perovskite Solar Cells," PRX Energy **1**(1), 013003 (2022).

[14] W. Clarke, L.J. Bennett, Y. Grudeva, J.M. Foster, G. Richardson, and N.E. Courtier, "IonMonger 2.0: software for free, fast and versatile simulation of current, voltage and impedance response of planar perovskite solar cells," J. Comput. Electron., (2022).

[15] M.T. Neukom, A. Schiller, S. Züfle, E. Knapp, J. Ávila, D. Pérez-del-Rey, C. Dreessen, K.P.S. Zanoni, M. Sessolo, H.J. Bolink, and B. Ruhstaller, "Consistent Device Simulation Model Describing Perovskite Solar Cells in Steady-State, Transient, and Frequency Domain," ACS Appl. Mater. Interfaces **11**(26), 23320–23328 (2019).

[16] D. Moia, I. Gelmetti, P. Calado, W. Fisher, M. Stringer, O. Game, Y. Hu, P. Docampo, D. Lidzey, E. Palomares, J. Nelson, and P.R.F. Barnes, "Ionic-to-electronic current amplification in hybrid perovskite solar cells: ionically gated transistor-interface circuit model explains hysteresis and impedance of mixed conducting devices," Energy Environ. Sci. **12**(4), 1296–1308 (2019).

[17] W. Clarke, M.V. Cowley, M.J. Wolf, P. Cameron, A. Walker, and G. Richardson, "Inverted hysteresis as a diagnostic tool for perovskite solar cells: Insights from the drift-diffusion model," J. Appl. Phys. **133**(9), 095001 (2023).

[18] L.J. Bennett, A.J. Riquelme, and J.A. Anta, "Avoiding ionic interference in the computation of ideality factor for perovskite solar cells and an analytical theory for their impedance spectroscopy response," (n.d.).

[19] N. Filipoiu, A.T. Preda, D.-V. Anghel, R. Patru, R.E. Brophy, M. Kateb, C. Besleaga, A.G. Tomulescu, I. Pintilie, A. Manolescu, and G.A. Nemnes, "Capacitive and Inductive Effects in Perovskite Solar Cells: The Different Roles of Ionic Current and Ionic Charge Accumulation," Phys. Rev. Appl. **18**(6), 064087 (2022).

[20] E. Ghahremanirad, A. Bou, S. Olyaee, and J. Bisquert, "Inductive Loop in the Impedance Response of Perovskite Solar Cells Explained by Surface Polarization Model," J. Phys. Chem. Lett. **8**(7), 1402–1406 (2017).

[21] J.S. Blakemore, "Approximations for Fermi-Dirac integrals, especially the function used to describe electron density in a semiconductor," Solid State Electron. **25**(11), 1067–1076 (1982).

[22] W. Shockley, and W.T. Read, "Statistics of the Recombinations of Holes and Electrons," Phys. Rev. **87**(5), 835–842 (1952).

[23] D.A. Van Nijen, M. Muttillo, R. Van Dyck, J. Poortmans, M. Zeman, O. Isabella, and P. Manganiello, "Revealing capacitive and inductive effects in modern industrial c-Si photovoltaic cells through impedance spectroscopy," Sol. Energy Mater. Sol. Cells **260**, 112486 (2023).

[24] C.J. Diliegros-Godines, O. García-Zaldívar, F.J. Flores-Ruiz, E. Fernández-Domínguez, G. Torres-Delgado, and R. Castanedo-Pérez, "Impedance spectroscopy of Au/Cu2Te/CdTe/CdS/Cd2SnO4/glass solar cells," Ceram. Int. **49**(4), 6699–6707 (2023).

[25] J. Bisquert, "Theory of the impedance of charge transfer via surface states in dye-sensitized solar cells," J. Electroanal. Chem. **646**(1–2), 43–51 (2010).

[26] I. Zarazua, J. Bisquert, and G. Garcia-Belmonte, "Light-Induced Space-Charge Accumulation Zone as Photovoltaic Mechanism in Perovskite Solar Cells," J. Phys. Chem. Lett. **7**(3), 525–528 (2016).

[27] I. Zarazua, G. Han, P.P. Boix, S. Mhaisalkar, F. Fabregat-Santiago, I. Mora-Seró, J. Bisquert, and G. Garcia-Belmonte, "Surface Recombination and Collection Efficiency in Perovskite Solar Cells from Impedance Analysis," J. Phys. Chem. Lett. **7**(24), 5105–5113 (2016).

[28] M.H. Futscher, M.K. Gangishetty, D.N. Congreve, and B. Ehrler, "Quantifying mobile ions and electronic defects in perovskite-based devices with temperature-dependent capacitance measurements: Frequency vs time domain," J. Chem. Phys. **152**(4), 044202 (2020).

[29] J. Bisquert, "Chemical capacitance of nanostructured semiconductors: its origin and significance for nanocomposite solar cells," Phys. Chem. Chem. Phys. **5**(24), 5360 (2003).

[30] S. Ravishankar, O. Almora, C. Echeverría-Arrondo, E. Ghahremanirad, C. Aranda, A. Guerrero, F. Fabregat-Santiago, A. Zaban, G. Garcia-Belmonte, and J. Bisquert, "Surface Polarization Model for the Dynamic Hysteresis of Perovskite Solar Cells," J. Phys. Chem. Lett. **8**(5), 915–921 (2017).

[31] A.O. Alvarez, R. Arcas, C.A. Aranda, L. Bethencourt, E. Mas-Marzá, M. Saliba, and F. Fabregat-Santiago, "Negative Capacitance and Inverted Hysteresis: Matching Features in Perovskite Solar Cells," J. Phys. Chem. Lett. **11**(19), 8417–8423 (2020).

[32] A. Lasia, "The Origin of the Constant Phase Element," J. Phys. Chem. Lett. **13**(2), 580–589 (2022).

[33] C. Gonzales, A. Guerrero, and J. Bisquert, "Transition from Capacitive to Inductive Hysteresis: A Neuron-Style Model to Correlate *I – V* Curves to Impedances of Metal Halide Perovskites," J. Phys. Chem. C **126**(32), 13560–13578 (2022).

[34] C.H. Hsu, and F. Mansfeld, "Technical Note: Concerning the Conversion of the Constant Phase Element Parameter Y0 into a Capacitance," Corros. 2001 57 9, 747–748 (n.d.).

[35] X. Zheng, Y. Hou, C. Bao, J. Yin, F. Yuan, Z. Huang, K. Song, J. Liu, J. Troughton, N. Gasparini, C. Zhou, Y. Lin, D.-J. Xue, B. Chen, A.K. Johnston, N. Wei, M.N. Hedhili, M. Wei, A.Y. Alsalloum, P. Maity, B. Turedi, C. Yang, D. Baran, T.D. Anthopoulos, Y. Han, Z.-H. Lu, O.F. Mohammed, F. Gao, E.H. Sargent, and O.M. Bakr, "Managing grains and interfaces via ligand anchoring enables 22.3%-efficiency inverted perovskite solar cells," Nat. Energy **5**(2), 131–140 (2020).

[36] J. Sun, C. Shou, J. Sun, X. Wang, Z. Yang, Y. Chen, J. Wu, W. Yang, H. Long, Z. Ying, X. Yang, J. Sheng, B. Yan, and J. Ye, "NiO-Seeded Self-Assembled Monolayers as Highly Hole-Selective Passivating Contacts for Efficient Inverted Perovskite Solar Cells," Sol. RRL **5**(11), 2100663 (2021).

[37] S. Chen, X. Xiao, H. Gu, and J. Huang, "Iodine reduction for reproducible and high-performance perovskite solar cells and modules," Sci. Adv. **7**(10), eabe8130 (2021).

[38] Z. Li, B. Li, X. Wu, S.A. Sheppard, S. Zhang, D. Gao, N.J. Long, and Z. Zhu, "Organometallic-functionalized interfaces for highly efficient inverted perovskite solar cells," Science **376**(6591), 416–420 (2022).

[39] H. Chen, S. Teale, B. Chen, Y. Hou, L. Grater, T. Zhu, K. Bertens, S.M. Park, H.R. Atapattu, Y. Gao, M. Wei, A.K. Johnston, Q. Zhou, K. Xu, D. Yu, C. Han, T. Cui, E.H. Jung, C. Zhou, W. Zhou, A.H. Proppe, S. Hoogland, F. Laquai, T. Filleter, K.R. Graham, Z. Ning, and E.H. Sargent, "Quantum-size-tuned heterostructures enable efficient and stable inverted perovskite solar cells," Nat. Photonics **16**(5), 352–358 (2022).

[40] Q. Jiang, J. Tong, Y. Xian, R.A. Kerner, S.P. Dunfield, C. Xiao, R.A. Scheidt, D. Kuciauskas, X. Wang, M.P. Hautzinger, R. Tirawat, M.C. Beard, D.P. Fenning, J.J. Berry, B.W. Larson, Y. Yan, and K. Zhu, "Surface reaction for efficient and stable inverted perovskite solar cells," Nature **611**(7935), 278–283 (2022).

[41] J. Yang, Q. Cao, T. Wang, B. Yang, X. Pu, Y. Zhang, H. Chen, I. Tojiboyev, Y. Li, L. Etgar, X. Li, and A. Hagfeldt, "Inhibiting metal-inward diffusion-induced degradation through strong chemical coordination toward stable and efficient inverted perovskite solar cells," Energy Environ. Sci. **15**(5), 2154–2163 (2022).

[42] M. Tutundzic, X. Zhang, S. Lammar, S. Singh, P. Marchezi, T. Merckx, A. Aguirre, E. Moons, T. Aernouts, Y. Kuang, and B. Vermang, "Toward Efficient and Fully Scalable Sputtered NiO_x -Based Inverted Perovskite Solar Modules via Co-Ordinated Modification Strategies," Sol. RRL **8**(3), 2300862 (2024).

[43] A. Harter, K. Artuk, F. Mathies, O. Karalis, H. Hempel, A. Al-Ashouri, S. Albrecht, R. Schlatmann, C. Ballif, B. Stannowski, and C.M. Wolff, "Perovskite/Silicon Tandem Solar Cells Above 30% Conversion Efficiency on Submicron-Sized Textured Czochralski-Silicon Bottom Cells with Improved Hole-Transport Layers," ACS Appl. Mater. Interfaces **16**(45), 62817–62826 (2024).

[44] J. Chen, X. Wang, T. Wang, J. Li, H.Y. Chia, H. Liang, S. Xi, S. Liu, X. Guo, R. Guo, Z. Jia, X. Yin, Q. Zhou, Y. Wang, Z. Shi, H. Zhou, D. Lai, M. Zhang, Z. Xing, W.R. Leow, W. Yan, and Y. Hou, "Determining the bonding–degradation trade-off at heterointerfaces for increased efficiency and stability of perovskite solar cells," Nat. Energy, (2024).

[45] J. Bisquert, "Interpretation of the Recombination Lifetime in Halide Perovskite Devices by Correlated Techniques," J. Phys. Chem. Lett. **13**(31), 7320–7335 (2022).

[46] S. Ravishankar, Z. Liu, Y. Wang, T. Kirchartz, and U. Rau, "How Charge Carrier Exchange between Absorber and Contact Influences Time Constants in the Frequency Domain Response of Perovskite Solar Cells," PRX Energy **2**(3), 033006 (2023).

[47] M. Taukeer Khan, F. Khan, A. Al-Ahmed, S. Ahmad, and F. Al-Sulaiman, "Evaluating the Capacitive Response in Metal Halide Perovskite Solar Cells," Chem. Rec. **22**(7), e202100330 (2022).

[48] A.J. Riquelme, K. Valadez-Villalobos, P.P. Boix, G. Oskam, I. Mora-Seró, and J.A. Anta, "Understanding equivalent circuits in perovskite solar cells. Insights from drift-diffusion simulation," Phys. Chem. Chem. Phys. **24**(26), 15657–15671 (2022).

[49] S.H. Bennett, J. Ghosh, E. Gros-Daillon, F. Lédée, J. Mayén Guillén, J.-M. Verilhac, J. Zaccaro, D.Y. Chung, V. Klepov, M.G. Kanatzidis, and P.J. Sellin, "Charge transport comparison of FA, MA and Cs lead halide perovskite single crystals for radiation detection," Front. Detect. Sci. Technol. **1**, (2023).

[50] J. Lim, M.T. Hörantner, N. Sakai, J.M. Ball, S. Mahesh, N.K. Noel, Y.-H. Lin, J.B. Patel, D.P. McMeekin, M.B. Johnston, B. Wenger, and H.J. Snaith, "Elucidating the long-range charge carrier mobility in metal halide perovskite thin films," Energy Environ. Sci. **12**(1), 169–176 (2019).

[51] A. Musiienko, F. Yang, T.W. Gries, C. Frasca, D. Friedrich, A. Al-Ashouri, E. Sağlamkaya, F. Lang, D. Kojda, Y.-T. Huang, V. Stacchini, R.L.Z. Hoye, M. Ahmadi, A. Kanak, and A. Abate, "Resolving electron and hole transport properties in semiconductor materials by constant light-induced magneto transport," Nat. Commun. **15**(1), 316 (2024).

[52] Y. Zhai, K. Wang, F. Zhang, C. Xiao, A.H. Rose, K. Zhu, and M.C. Beard, "Individual Electron and Hole Mobilities in Lead-Halide Perovskites Revealed by Noncontact Methods," ACS Energy Lett. **5**(1), 47–55 (2020).